Profile of the Static Permittivity Tensor of Water at Interfaces: Consequences for Capacitance, Hydration Interaction and Ion Adsorption

Douwe Jan Bonthuis[1], Stephan Gekle[1] & Roland R. Netz[2]

[1]Physik Department, Technische Universität München, 85748 Garching, Germany
[2]Fachbereich Physik, Freie Universität Berlin, 14195 Berlin, Germany

► **Abstract.** We derive the theoretical framework to calculate the dielectric response tensor and determine its components for water adjacent to hydrophilic and hydrophobic surfaces using molecular dynamics simulations. For the nonpolarizable water model used, linear response theory is found to be applicable up to an external perpendicular field strength of ~ 2 V/nm, well beyond the experimental dielectric breakdown threshold. The dipole contribution dominates the dielectric response parallel to the interface, whereas for the perpendicular component it is essential to keep the quadrupole and octupole terms. Including the space-dependent dielectric function in a mean-field description of the ion distribution at a single charged interface, we reproduce experimental values of the interfacial capacitance. At the same time, the dielectric function decreases the electrostatic part of the disjoining pressure between two charged surfaces, unlike previously thought. The difference in interfacial polarizability between hydrophilic and hydrophobic surfaces can be quantized in terms of the dielectric dividing surface. Using the dielectric dividing surface and the Gibbs dividing surface positions to estimate the free energy of a single ion close to an interface, ion specific adsorption effects are found to be more pronounced at hydrophobic surfaces compared to hydrophilic ones, in agreement with experimental trends.

1 Introduction

Electrostatic interactions between charged objects in aqueous solution, such as lipid membranes, proteins and ions, are profoundly influenced by the surrounding water [1]. Each charge embedded in the dielectric environment of the water couples to the local electric field, which comprises both the displacement field emanating from the charged objects and the polarization field stemming from the dielectric medium. In a macroscopic approach, the effect of the water on electrostatic interactions is quantified by means of the static dielectric tensor ε, which is spatially constant and diagonal in bulk. Close to an interface, however, the effect of the water is more intricate. The water density near an interface strongly deviates from its bulk value and the proximity of a surface restricts the molecular dynamics [2]. Short-ranged interactions between macroscopic objects in water that go beyond homogeneous continuum electrostatics, such as hydration forces and hydrophobic effects, are often attributed to this local variation of the solvent structure [3, 4]. Because of the extremely polar nature of water molecules, the water structure directly affects the electrostatic environment, making the dielectric tensor inherently space-dependent. The effect of the solvent structure strongly depends on the nature of the interface: hydrophobic and hydrophilic surfaces have a vastly different influence on the adjacent water [5, 6].

Within the framework of linear response theory, the space-dependent dielectric response function can be expressed as a nonlocal tensor, depending on the positions of the source and the response [7, 8, 9]. In Fourier space, the nonlocal dielectric tensor of bulk water exhibits two singularities for wave vectors at molecular length scales [10]. Whether similar anomalies appear in the space-dependent static dielectric function of interfacial water has long remained unclear.

The capacitance formed by a charged interface and its counterions serves as a sensitive probe for measuring dielectric interface effects. It has been known for almost a century that the Gouy-Chapman model overestimates experimental data of the interfacial capacitance, which has been ascribed to variation of the dielectric constant at the interface [11, 12]. In the Stern model of the electric double layer, the variation of the dielectric tensor is accounted for by the combination of a length scale and an effective interfacial dielectric constant, reproducing the experimental capacitance [13]. In the limit of low salt concentration, it has been shown how the Stern layer contribution to the capacitance emerges from the introduction of a nonlocal dielectric function, independent of the exact form of the dielectric profile [7]. The relation between the dielectric profile and the length scale appearing in the Stern model has been established as well [8]. Only recently however, have we explicitly calculated the interfacial dielectric profile of pure water [14].

The question of whether the decrease of the dielectric profile reflects ionic or rather intrinsic water properties is

still subject to debate. The decrease of the dielectric constant has been attributed to the high ionic concentration close to charged interfaces [15] or to dielectric saturation due to the corresponding high electric field strength [16]. However, recent terahertz spectroscopy experiments on carbohydrates [17] and lipid membranes [18] have shown that the dielectric response of water itself is modified within an interfacial layer of molecular size. Theoretical attempts to relate the dielectric response to molecular dynamics have been based on analytic as well as simulation studies. Analytic approaches include approximate statistical mechanical methods, which have been used to show that the reduced dielectric constant at the interface is associated with molecular ordering and orientation [19]. In another analytic approach, water polarization has been included explicitly in a mean-field description [20, 21], where molecular effects such as the abovementioned singularities are not accounted for. Simulations with explicit water and ions did not allow for straightforward interpretation previously, partly because of the appearance of higher-order multipole moments. In fact, the preferred orientation of water molecules near an interface is set by the fundamental asymmetry stemming from the quadrupole and higher-order even multipole moments [22, 23, 24]. This asymmetrical water structure plays a decisive role in the dielectric response of water at an interface, which is ignored in many studies [25]. Recently, we have shown that the electric quadrupole and octupole moments are essential components of the interfacial dielectric function [14].

The dielectric function in thin interfacial layers strongly affects the forces between macromolecules and surfaces as a result of the long range of the electrostatic force. Furthermore, a knowledge of the space-dependent dielectric tensor is indispensable for the interpretation of the ionic surface propensity [26] and solvation free energy [27, 28, 29], as well as the electrophoretic mobility of solutes and the double-layer capacitance [11, 12]. In addition, the dielectric tensor is a vital ingredient for coarse-grained calculations, where the water is taken into account implicitly. Finally, the electrostatics close to a solid interface are crucial from a technological point of view, in particular for the design of novel energy storage media based on the double-layer capacitance.

In this paper, we thoroughly investigate the consequences of the interfacial dielectric profile for the interfacial capacitance, the hydration interaction between charged plates in water, and the ion adsorption energy at hydrophilic and hydrophobic surfaces. First, we present a complete derivation of the expressions to calculate the components of the dielectric response tensor at planar interfaces from molecular dynamics simulations. Second, we calculate the dielectric tensor of pure water adjacent to both hydrophilic (hydroxyl-terminated) and hydrophobic (hydrogen-terminated) diamond surfaces. We show that the salient differences between the two surface types can be quantified in terms of a single length scale, set by the position of the dielectric dividing surface. Third, we investigate the effect of the higher-order electric moments on the electric potential profile across the interface. Fourth, we incorporate the space dependence of the dielectric tensor in a Poisson-Boltzmann description of a salt solution at a charged interface. Comparing with experimental values, we show that including the dielectric response of pure water suffices to capture the dependence of the double-layer capacitance on the salt concentration. Fifth, we calculate the disjoining pressure between two charged surfaces using the same Poisson-Boltzmann description. On the Poisson-Boltzmann level, the dielectric profile appears to be insufficient to describe the strong short-ranged repulsive forces commonly measured between both charged and uncharged surfaces in water [30]. Finally, we estimate the free energy of a single ion near a dielectric boundary and show that the different dielectric characteristics of hydrophilic and hydrophobic surfaces have a pronounced effect on ion adsorption. A partial account of the work described in this paper has been published in Ref. [14]. All equations are given in SI units.

2 Theoretical Framework

► **Linear response.** In the most general sense, the dielectric response function depends on the position $\boldsymbol{r}$ of the displacement field $\boldsymbol{D}(\boldsymbol{r})$, the position $\boldsymbol{r}'$ of the local electric field $\boldsymbol{E}(\boldsymbol{r}')$ and on the magnitude of the field. In the linear response regime, a change in the displacement field is linearly related to a change in the electric field,

$$\Delta\boldsymbol{D}(\boldsymbol{r}) = \varepsilon_0 \int \varepsilon_{\mathrm{nl}}(\boldsymbol{r},\boldsymbol{r}') \cdot \Delta\boldsymbol{E}(\boldsymbol{r}')\, \mathrm{d}\boldsymbol{r}', \tag{1}$$

with ε_0 being the permittivity of vacuum and $\varepsilon_{\mathrm{nl}}(\boldsymbol{r},\boldsymbol{r}')$ being the nonlocal dielectric tensor. If the electric field is constant in space, $\Delta\boldsymbol{E}(\boldsymbol{r}) = \Delta\boldsymbol{E}$, the response function is automatically local,

$$\Delta\boldsymbol{D}(\boldsymbol{r}) = \varepsilon_0 \varepsilon(\boldsymbol{r}) \cdot \Delta\boldsymbol{E} \quad \text{with} \quad \varepsilon(\boldsymbol{r}) = \int \varepsilon_{\mathrm{nl}}(\boldsymbol{r},\boldsymbol{r}')\, \mathrm{d}\boldsymbol{r}', \tag{2}$$

making the usual locality assumption $\varepsilon_{\mathrm{nl}}(\boldsymbol{r},\boldsymbol{r}') = \varepsilon(\boldsymbol{r})\,\delta(\boldsymbol{r}-\boldsymbol{r}')$ superfluous. Alternatively, the inverse dielectric response function is defined by [7]

$$\Delta\boldsymbol{E}(\boldsymbol{r}) = \varepsilon_0^{-1} \int \varepsilon_{\mathrm{nl}}^{-1}(\boldsymbol{r},\boldsymbol{r}') \cdot \Delta\boldsymbol{D}(\boldsymbol{r}')\, \mathrm{d}\boldsymbol{r}', \tag{3}$$

with $\varepsilon_{\mathrm{nl}}^{-1}(\boldsymbol{r},\boldsymbol{r}')$ being the functional inverse of $\varepsilon_{\mathrm{nl}}(\boldsymbol{r},\boldsymbol{r}')$, defined by $\int \varepsilon_{\mathrm{nl}}(\boldsymbol{r},\boldsymbol{r}')\,\varepsilon_{\mathrm{nl}}^{-1}(\boldsymbol{r}',\boldsymbol{r}'')\,\mathrm{d}\boldsymbol{r}' = \delta(\boldsymbol{r}-\boldsymbol{r}'')$. The inverse dielectric response function is automatically local when the displacement field is constant in space, yielding

$$\Delta\boldsymbol{E}(\boldsymbol{r}) = \varepsilon_0^{-1}\varepsilon^{-1}(\boldsymbol{r}) \cdot \Delta\boldsymbol{D}, \tag{4}$$

with $\varepsilon^{-1}(\boldsymbol{r})$ being the inverse dielectric function. Note that the relation $\varepsilon(\boldsymbol{r})\,\varepsilon^{-1}(\boldsymbol{r}) = \mathbb{1}$ does not hold without additional assumptions.

► **Multipole expansion.** In a classical approximation, the polar molecules are regarded as being composed of atoms, located at positions $\boldsymbol{r}_j^i$, carrying point charges q_j^i. The total charge density $\rho(\boldsymbol{r})$ is given by averaging over the partial charges q_j^i of all atoms $j\,(i)$ and all molecules i,

$$\rho(\boldsymbol{r}) = \sum_i \sum_{j(i)} q_j^i\,\delta\left(\boldsymbol{r} - \boldsymbol{r}_j^i\right). \tag{5}$$

We will now expand the electric field in terms of molecular multipole moments, starting from the integral equation for the electric field [31],

$$\varepsilon_0 \boldsymbol{E}(\boldsymbol{r}) = \frac{1}{4\pi}\int \rho(\boldsymbol{r}')\,\frac{\boldsymbol{r}-\boldsymbol{r}'}{|\boldsymbol{r}-\boldsymbol{r}'|^3}\,\mathrm{d}\boldsymbol{r}'. \tag{6}$$

After inserting Eq. 5, the integration variable is shifted from $\boldsymbol{r}'$ to $\boldsymbol{r}' + \boldsymbol{r}_j^i - \boldsymbol{r}_i$, leading to

$$\varepsilon_0 \boldsymbol{E}(\boldsymbol{r}) = \frac{1}{4\pi}\int \sum_i \sum_{j(i)} q_j^i \delta(\boldsymbol{r}' - \boldsymbol{r}_i) \times \frac{(\boldsymbol{r}-\boldsymbol{r}') - \left(\boldsymbol{r}_j^i - \boldsymbol{r}_i\right)}{|\,(\boldsymbol{r}-\boldsymbol{r}') - \left(\boldsymbol{r}_j^i - \boldsymbol{r}_i\right)|^3}\,\mathrm{d}\boldsymbol{r}', \tag{7}$$

where $\boldsymbol{r}_i$ is some arbitrary reference position in the molecule. The fraction in Eq. 7 is then expanded for the case where the intramolecular distance $\boldsymbol{r}_j^i - \boldsymbol{r}_i$ is much smaller than the distance between charge and field points $\boldsymbol{r} - \boldsymbol{r}'$,

$$\varepsilon_0 \boldsymbol{E}(\boldsymbol{r}) = \frac{1}{4\pi}\int \sum_i \sum_{j(i)} q_j^i \delta(\boldsymbol{r}' - \boldsymbol{r}_i) \times \left[\frac{\boldsymbol{r}-\boldsymbol{r}'}{|\boldsymbol{r}-\boldsymbol{r}'|^3} + \left(\boldsymbol{r}_j^i - \boldsymbol{r}_i\right)\cdot\nabla'\frac{\boldsymbol{r}-\boldsymbol{r}'}{|\boldsymbol{r}-\boldsymbol{r}'|^3} + \frac{1}{2}\left(\boldsymbol{r}_j^i - \boldsymbol{r}_i\right)\left(\boldsymbol{r}_j^i - \boldsymbol{r}_i\right) : \nabla'\nabla'\frac{\boldsymbol{r}-\boldsymbol{r}'}{|\boldsymbol{r}-\boldsymbol{r}'|^3} + \ldots\right]\mathrm{d}\boldsymbol{r}', \tag{8}$$

where the minus sign of $-\left(\boldsymbol{r}_j^i - \boldsymbol{r}_i\right)$ cancels the minus sign of $\nabla'(\boldsymbol{r}-\boldsymbol{r}') = -\nabla(\boldsymbol{r}-\boldsymbol{r}')$. Next, all gradient terms are integrated by parts,

$$\varepsilon_0 \boldsymbol{E}(\boldsymbol{r}) = \frac{1}{4\pi}\int \frac{\boldsymbol{r}-\boldsymbol{r}'}{|\boldsymbol{r}-\boldsymbol{r}'|^3}\left[\sum_i\sum_{j(i)} q_j^i\delta(\boldsymbol{r}'-\boldsymbol{r}_i) - \nabla'\cdot\sum_i\sum_{j(i)} q_j^i\delta(\boldsymbol{r}'-\boldsymbol{r}_i)\left(\boldsymbol{r}_j^i-\boldsymbol{r}_i\right) + \frac{1}{2}\nabla'\nabla' : \sum_i\sum_{j(i)} q_j^i\delta(\boldsymbol{r}'-\boldsymbol{r}_i)\left(\boldsymbol{r}_j^i-\boldsymbol{r}_i\right)\left(\boldsymbol{r}_j^i-\boldsymbol{r}_i\right) - \ldots\right]\mathrm{d}\boldsymbol{r}'. \tag{9}$$

The separate components appearing in Eq. 9 can be expressed in terms of the molecular multipole moments of order $l \in \{0, 1, 2, \ldots\}$, which are defined as

$$\mathsf{p}_{li} = \frac{1}{l!}\sum_{j(i)} q_j^i \left(\boldsymbol{r}_j^i - \boldsymbol{r}_i\right)^l, \tag{10}$$

with j running over all partial charges q_j^i of molecule i. The power inside the summation is understood as a serial direct vector multiplication, making p_{li} a tensor of rank l. The density of each multipole moment is defined as

$$\mathsf{P}_l(\boldsymbol{r}) = \sum_i \mathsf{p}_{li}\,\delta(\boldsymbol{r}-\boldsymbol{r}_i), \tag{11}$$

where the summation is carried out over all molecules [32]. Using Eqs. 10 and 11, Eq. 9 becomes

$$\varepsilon_0 \boldsymbol{E}(\boldsymbol{r}) = \frac{1}{4\pi}\int \frac{\boldsymbol{r}-\boldsymbol{r}'}{|\boldsymbol{r}-\boldsymbol{r}'|^3}\times \left[P_0(\boldsymbol{r}') - \nabla'\cdot\boldsymbol{P}_1(\boldsymbol{r}') + \nabla'\nabla' : \mathsf{P}_2(\boldsymbol{r}') - \ldots\right]\mathrm{d}\boldsymbol{r}'. \tag{12}$$

We use the identity

$$\nabla\cdot\frac{\boldsymbol{r}-\boldsymbol{r}'}{|\boldsymbol{r}-\boldsymbol{r}'|^3} = 4\pi\delta(\boldsymbol{r}-\boldsymbol{r}') \tag{13}$$

to perform the integrals in Eq. 12, except for the P_0 term, to which we will come back later. The divergence of Eq. 12 equals

$$\nabla\cdot\varepsilon_0\boldsymbol{E}(\boldsymbol{r}) = \nabla\cdot\frac{1}{4\pi}\int P_0(\boldsymbol{r}')\,\frac{\boldsymbol{r}-\boldsymbol{r}'}{|\boldsymbol{r}-\boldsymbol{r}'|^3}\,\mathrm{d}\boldsymbol{r}' + \left[-\nabla\cdot\boldsymbol{P}_1(\boldsymbol{r}) + \nabla\nabla : \mathsf{P}_2(\boldsymbol{r}) - \ldots\right], \tag{14}$$

from which the electric field $\boldsymbol{E}(\boldsymbol{r})$ follows as

$$\varepsilon_0\boldsymbol{E}(\boldsymbol{r}) = \boldsymbol{D}(\boldsymbol{r}) - \boldsymbol{m}(\boldsymbol{r}). \tag{15}$$

The first term in the expansion on the right-hand side of Eq. 15 is the monopole term,

$$\boldsymbol{D}(\boldsymbol{r}) = \frac{1}{4\pi}\int P_0(\boldsymbol{r}')\,\frac{\boldsymbol{r}-\boldsymbol{r}'}{|\boldsymbol{r}-\boldsymbol{r}'|^3}\,\mathrm{d}\boldsymbol{r}', \tag{16}$$

corresponding to the field from the free charges. The second term is the total polarization density $\boldsymbol{m}(\boldsymbol{r})$,

$$\boldsymbol{m}(\boldsymbol{r}) = \boldsymbol{P}_1(\boldsymbol{r}) - \nabla\cdot\mathsf{P}_2(\boldsymbol{r}) + \nabla\nabla : \mathsf{P}_3(\boldsymbol{r}) - \ldots, \tag{17}$$

which comprises contributions from the dipole moment per unit volume $\boldsymbol{P}_1$, quadrupole moment P_2, octupole moment P_3 and all higher-order moments. When the polarization is calculated in basic electrostatics, all multipole terms of order higher than the dipole are often neglected [31], which is exact for a Stockmayer fluid, for example, where each molecule carries an ideal dipole. For water however, the higher-order terms are of major

importance. Note that we could also calculate the multipole moments from all individual atoms instead of averaging an expansion in molecular multipole moments. Although both descriptions of the electrostatics are equivalent, clustering the atoms first to calculate molecular multipole moments has the advantage of a vanishing monopole moment in the case of neutral molecules.

► **Fluctuation-dissipation theorem.** To estimate the dielectric function from the polarization fluctuations, we write a statistical mechanical expression for the ensemble average excess polarization. The total interaction energy of a water-filled volume $\mathcal{V}$ in absence of an external electric field is denoted $U(X)$, with X all relevant coordinates. The energy change ΔU upon application of an external electric field is given by the coupling of the polarization to the field $\boldsymbol{F}$ inside the dielectric,

$$\Delta U = \int_{\mathcal{V}} \psi(\boldsymbol{r})\, \rho(\boldsymbol{r})\, \mathrm{d}\boldsymbol{r}, \tag{18}$$

with ψ being the excess potential caused by the field, $\nabla\psi(\boldsymbol{r}) = -\boldsymbol{F}$, and $\rho(\boldsymbol{r}) = \varepsilon_0 \nabla \cdot \boldsymbol{E}(\boldsymbol{r})$ being the total charge density. The field $\boldsymbol{F}$ to which the fluid responds is constant in space. Therefore, $\boldsymbol{F}$ is associated with either $\boldsymbol{E}$ or $\boldsymbol{D}/\varepsilon_0$ depending on the boundary conditions. After one partial integration, the excess energy is given by

$$\Delta U = -\int_{\mathcal{V}} \nabla\psi(\boldsymbol{r}) \cdot \varepsilon_0 \boldsymbol{E}(\boldsymbol{r})\, \mathrm{d}\boldsymbol{r} = -\int_{\mathcal{V}} \boldsymbol{F} \cdot \boldsymbol{m}(\boldsymbol{r})\, \mathrm{d}\boldsymbol{r}, \tag{19}$$

where we used that $\varepsilon_0 \boldsymbol{E}(\boldsymbol{r}) = -\boldsymbol{m}(\boldsymbol{r})$ in the absence of free charges. Defining the total polarization by

$$\boldsymbol{M} = \int_{\mathcal{V}} \boldsymbol{m}(\boldsymbol{r})\, \mathrm{d}\boldsymbol{r}, \tag{20}$$

the excess polarization density upon application of the external field $\boldsymbol{F}$ is given by [33, 34, 35]

$$\begin{aligned} \Delta\boldsymbol{m} &= \langle \boldsymbol{m} \rangle_{\boldsymbol{F}} - \langle \boldsymbol{m} \rangle_0 \\ &= \frac{\int (\boldsymbol{m} - \langle \boldsymbol{m} \rangle_0) \exp\left[-\beta\left(U - \boldsymbol{M}\cdot\boldsymbol{F}\right)\right] \mathrm{d}X}{\int \exp\left[-\beta\left(U - \boldsymbol{M}\cdot\boldsymbol{F}\right)\right] \mathrm{d}X}, \end{aligned} \tag{21}$$

where $\langle \ldots \rangle_{\boldsymbol{F}}$ and $\langle \ldots \rangle_0$ denote the ensemble average with and without applied electric field, respectively. For molecules without atomic polarizability, the phase space over which the integration in Eq. 21 is performed consists of the positions $\boldsymbol{r}_i$ and orientations Ω_i of the permanent multipole moments, $\mathrm{d}X = \prod_i \mathrm{d}\boldsymbol{r}_i \mathrm{d}\Omega_i$, with i being the molecular index. For a small field $\boldsymbol{F}$, Eq. 21 can be linearized to yield

$$\Delta\boldsymbol{m} \approx \frac{\int (\boldsymbol{m} - \langle \boldsymbol{m} \rangle_0)\left(1 + \beta \boldsymbol{M}\cdot\boldsymbol{F}\right) \exp\left[-\beta U\right] \mathrm{d}X}{\int \exp\left[-\beta U\right] \mathrm{d}X}. \tag{22}$$

Using short-hand notation for the ensemble averages, we obtain the excess polarization vector as

$$\Delta\boldsymbol{m}(\boldsymbol{r}) \approx \beta\left[\langle \boldsymbol{m}(\boldsymbol{r})\, \boldsymbol{M}\rangle_0 - \langle \boldsymbol{m}(\boldsymbol{r})\rangle_0 \langle \boldsymbol{M}\rangle_0\right] \cdot \boldsymbol{F}. \tag{23}$$

The term in brackets in Eq. 23 includes all nine components of the fluctuation tensor.

► **Boundary conditions.** In a planar system with translational invariance in the x and y directions and a dielectric discontinuity in z direction, the dielectric tensor is diagonal with only two unique components: one parallel and one perpendicular to the surface. Additionally, the electric field and the polarization density depend only on the z direction. Maxwell's equation $\nabla \times \boldsymbol{E}(z) = 0$ implies

$$\nabla_z E_x(z) = \nabla_z E_y(z) = 0, \tag{24}$$

so that $E_\parallel$, corresponding to E_x or E_y, is independent of z everywhere. Using Eq. 2, Eq. 15 and the symmetry condition $\Delta E_\parallel = E_\parallel$ gives

$$\varepsilon_\parallel(z) = 1 + \frac{\Delta m_\parallel(z)}{\varepsilon_0 E_\parallel}. \tag{25}$$

The constant field $F_\parallel$ in Eq. 23 must correspond to the constant field $E_\parallel$. Therefore, combining Eqs. 23 and 25 leads to

$$\varepsilon_\parallel(z) \approx 1 + \varepsilon_0^{-1}\beta\left[\langle m_\parallel(z)\, M_\parallel\rangle_0 - \langle m_\parallel(z)\rangle_0 \langle M_\parallel\rangle_0\right]. \tag{26}$$

Now we turn to the perpendicular component $\varepsilon_\perp(z)$. Maxwell's equation for the displacement field, $\nabla\cdot\boldsymbol{D}(z) = P_0(z)$, shows that the displacement field is constant in space when $P_0(z) = 0$. Using the boundary condition $\Delta D_\perp(z) = D_\perp$, the inverse dielectric function given in Eq. 4 becomes

$$\varepsilon_\perp^{-1}(z) = 1 - \frac{\Delta m_\perp(z)}{D_\perp}. \tag{27}$$

In the perpendicular case, the spatially constant field $F_\perp$ must be associated with the constant displacement field $D_\perp/\varepsilon_0$. Consequently, by combining Eqs. 15, 23 & 27 we arrive at the fluctuation equation for the inverse perpendicular permittivity,

$$\varepsilon_\perp^{-1}(z) \approx 1 - \varepsilon_0^{-1}\beta\left[\langle m_\perp(z)\, M_\perp\rangle_0 - \langle m_\perp(z)\rangle_0 \langle M_\perp\rangle_0\right]. \tag{28}$$

When we apply an external electric field, the dielectric tensor can be determined directly using Eqs. 25 & 27. Eqs. 26 & 28 can be used when considering the fluctuations in the absence of an external electric field instead.

► **Calculation of the polarization density.** The perpendicular electric field is calculated from an integral over all charges,

$$E_\perp(z) = E_\perp(0) + \int_0^z \frac{\rho(z')}{\varepsilon_0}\, \mathrm{d}z'. \tag{29}$$

In Eq. 29, $E_\perp(0)$ is the external electric field. Using $\boldsymbol{m}(0) = 0$ and Eq. 15 with the fact that $D_\perp$ is constant, we find the equation for the perpendicular polarization density

$$m_\perp(z) = -\int_0^z \rho(z')\, \mathrm{d}z'. \tag{30}$$

To derive an expression for the parallel polarization, we virtually cut out a volume from the simulation box. In the following, we adopt two different, but equivalent viewpoints. First, we consider all partial charges on the atoms of each molecule explicitly. By cutting the volume, some water molecules are split, forming a nonzero monopole density $P_0(\boldsymbol{r})$ on either side of the virtual cut. In the second viewpoint, idealized multipole moments are located at a single point within each molecule, and the multipole moments are not affected by cutting.

According to the first viewpoint, the net charge inside the volume that has been carved out comprises only $P_0(\boldsymbol{r})$, stemming from the water molecules that have been split by cutting the volume, because the intact water molecules carry no net charge. Since the split water molecules are all located near the surface of the volume, the integrated charge takes the form of a surface charge,

$$\int_{\mathcal{V}} \rho(\boldsymbol{r})\, \mathrm{d}\boldsymbol{r} = \oint_{\partial\mathcal{V}} \sigma(\boldsymbol{r})\, \mathrm{d}\boldsymbol{r}, \tag{31}$$

with $\sigma(\boldsymbol{r})$ being the surface charge density arising from $P_0(\boldsymbol{r})$.

Adopting the second viewpoint, the total charge inside the volume is calculated from the polarization,

$$\int_{\mathcal{V}} \rho(\boldsymbol{r})\, \mathrm{d}\boldsymbol{r} = -\int_{\mathcal{V}} \nabla\cdot\boldsymbol{m}(\boldsymbol{r})\, \mathrm{d}\boldsymbol{r}, \tag{32}$$

which can be transformed into a surface integral,

$$\int_{\mathcal{V}} \rho(\boldsymbol{r})\, \mathrm{d}\boldsymbol{r} = -\oint_{\partial\mathcal{V}} \boldsymbol{m}(\boldsymbol{r})\cdot\hat{\boldsymbol{n}}\, \mathrm{d}\boldsymbol{r}. \tag{33}$$

Realizing that Eqs. 31 and 33 hold for any volume $\mathcal{V}$, we find $\sigma(\boldsymbol{r}) = -\boldsymbol{m}(\boldsymbol{r})\cdot\hat{\boldsymbol{n}}$. To calculate the polarization in x direction, we introduce a virtual cut perpendicular to the x axis. We only cut the water molecules at the position of the virtual cut, closing the volume without cutting any other molecules. The surface charge density resulting from the split water molecules equals

$$\sigma(z) = \int P_0(x,z)\, \mathrm{d}x, \tag{34}$$

where the x-dependence of $P_0(x,z)$ has the form of a dirac delta function at the position of the cut. Along the surface of the cut, $\boldsymbol{m}(z)\cdot\hat{\boldsymbol{n}} = \pm m_{\parallel}(z)$, and thus

$$m_{\parallel}(z) = \mp\int P_0(x,z)\, \mathrm{d}x, \tag{35}$$

where the different signs apply to closing the volume and integrating $P_0(x,z)$ on the different sides of the cut. To calculate $m_{\parallel}(z)$, Eq. 35 is averaged over many different cut positions along the x axis.

The polarization density components from Eqs. 30 and 35 are used directly to calculate the components of the dielectric response tensor. Alternatively, the polarization density is estimated from the expansion of Eq. 17,

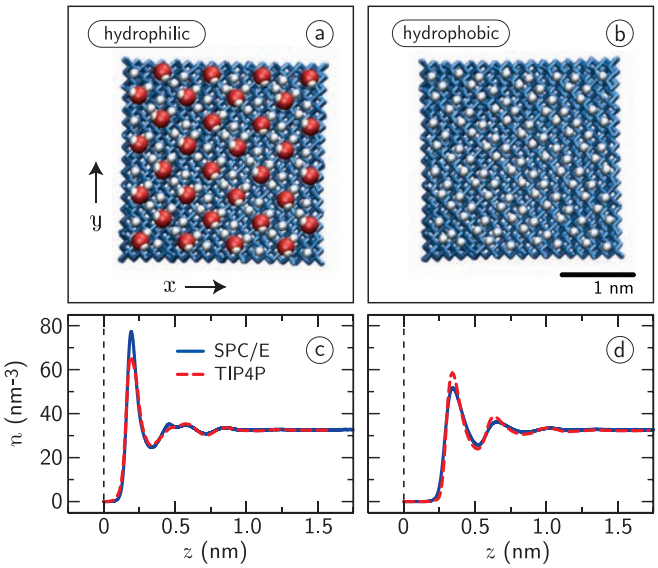

Figure 1: Topview of the two diamond surfaces: (a) hydrophilic (hydroxyl-terminated) and (b) hydrophobic (hydrogen-terminated). The oxygen atoms are shown in red, the hydrogen in white and the carbon in blue. (c)–(d) Corresponding molecular density profiles $n(z)$ of two different water models: SPC/E (blue solid lines) and TIP4P/2005 (red dashed lines), in absence of an external field.

where the multipole densities are calculated explicitly according to Eqs. 10 and 11. For this alternative method, we calculate the contributions up to the octupole term. Higher-order terms cannot be calculated from the simulations with sufficient accuracy. The molecular multipole moments of Eq. 10 are calculated with respect to the position of the oxygen atom.

3 Simulations & Results

► **Simulation setup.** We perform molecular dynamics simulations of pure SPC/E water in contact with a diamond slab consisting of a double FCC lattice of carbon atoms using the GROMACS molecular dynamics simulation package [36]. The primary cell contains 928 water molecules and we employ periodic boundary conditions in all directions. The carbon-water interaction is determined by the Lennard-Jones parameters $\sigma_{\mathrm{CW}} = 0.3367$ nm and $\epsilon_{\mathrm{CW}} = 0.4247$ kJ/mol (GROMOS 96). We study two surface types: one terminated with hydroxyl groups, giving a hydrophilic surface, and one terminated with hydrogen atoms, giving a hydrophobic surface. On the hydrophilic surface, one in four terminal atoms of the diamond has a hydroxyl group attached, corresponding to a surface coverage of $x_{\mathrm{OH}} = 1/4$ in the notation of Ref. [37]. The hydroxyl groups are free to rotate. The hydrogen atoms terminating the hydrophobic diamond have neither Lennard-Jones coefficients nor charge. The hydrogen atoms of the hydroxyl-terminated

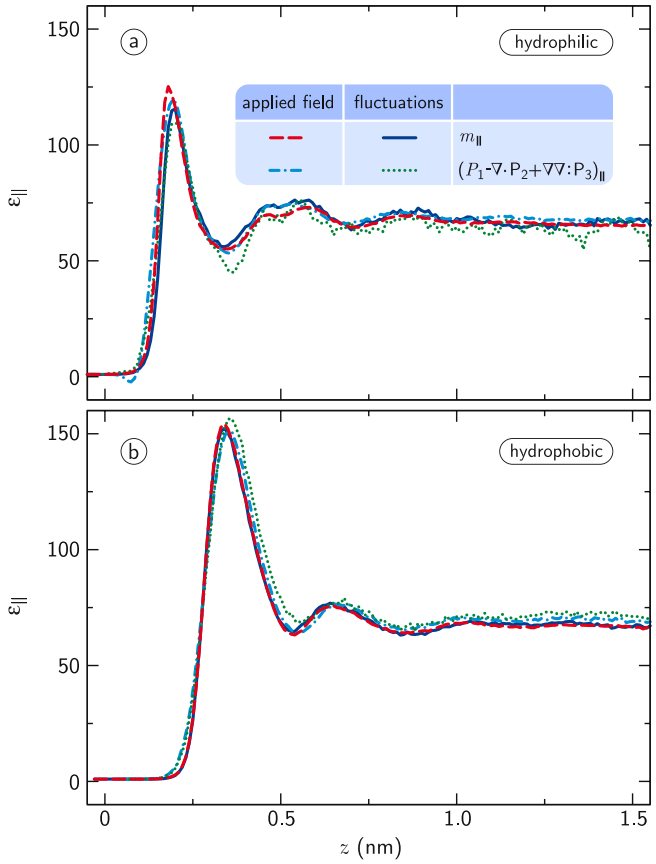

Figure 2: The parallel dielectric function $\varepsilon_\parallel(z)$ next to (a) the hydrophilic and (b) the hydrophobic diamond, calculated from the total polarization $m_\parallel(z)$ (Eq. 35) and from an explicit expansion of the polarization up to the octupole term (Eq. 17). The response is calculated in two different ways: from the excess polarization $\Delta m_\parallel(z)$ resulting from an applied external electric field in parallel direction of $E_\parallel = 0.05$ V/nm (Eq. 25) and from polarization fluctuations (Eq. 26).

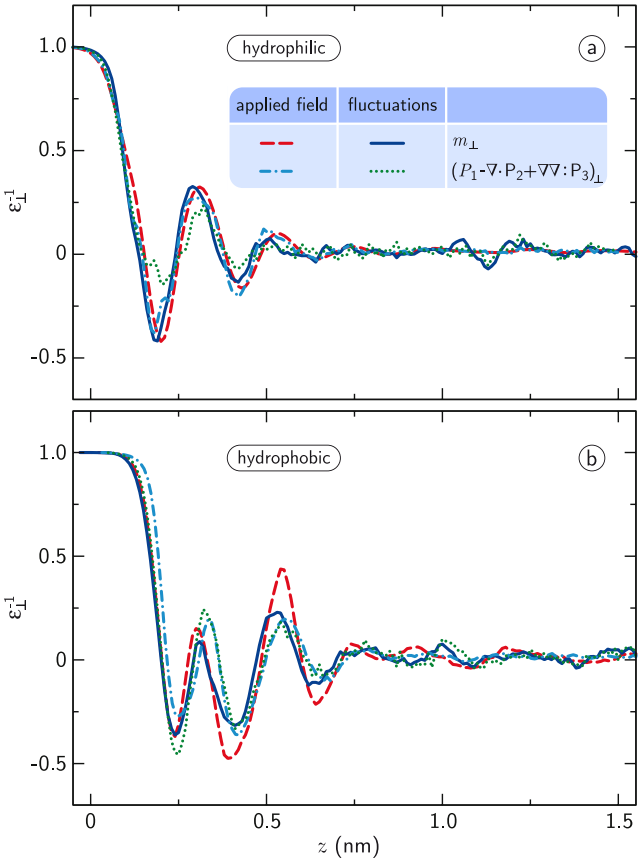

Figure 3: The inverse perpendicular dielectric function $\varepsilon_\perp^{-1}(z)$ next to (a) the hydrophilic and (b) the hydrophobic diamond, calculated from the total polarization $m_\perp(z)$ (Eq. 30) and from an explicit expansion of the polarization up to the octupole term (Eq. 17). The response is calculated in two different ways: from the excess polarization $\Delta m_\perp(z)$ resulting from an applied external displacement field in perpendicular direction (Eq. 27) and from polarization fluctuations (Eq. 28). For the curves corresponding to the total polarization, the applied field is $D_\perp/\varepsilon_0 = 0.5$ V/nm. The curves corresponding to the explicit expansion (dash-dotted lines) have been averaged over external field strengths of $D_\perp/\varepsilon_0 = 2.0$, 4.0 and 8.0 V/nm.

carbon atoms on the hydrophilic surface carry a partial charge of 0.408 e, the oxygen atoms carry -0.674 e and the connecting carbon atoms carry 0.266 e. The Lennard-Jones parameters of the oxide-water interaction are $\sigma_{\mathrm{ow}} = 0.3017$ nm and $\epsilon_{\mathrm{ow}} = 0.8070$ kJ/mol, and the hydrogen atoms have no Lennard-Jones interaction. Images of the two surface types are shown in Fig. 1 (a)–(b). For the hydrophilic surface, the position $z = 0$ is defined as the position of the oxygen atoms of the hydroxyl groups, whereas for the hydrophobic surfaces it corresponds to the position of the outermost carbon atoms. We simulate both surface types at vanishing external electric field for a total time of 80 ns, and at field strengths of $E_\parallel = 0.05$ V/nm in parallel direction and $D_\perp/\varepsilon_0 = 0.5$, 1.0, 2.0, 4.0 and 8.0 V/nm in perpendicular direction for a total time of $35 - 60$ ns. Simulations at the hydrophilic interface up to 1.0 V/nm and at the hydrophobic interface at 0.5 V/nm are run at constant pressure, using a semi-isotropic Berendsen barostat. Simulations at higher field strength are run at constant volume. The Lennard-Jones interaction is truncated at 1.0 nm using a shifted cutoff scheme. The Coulomb force is treated using a real-space cutoff at 1.2 nm and pseudo-two-dimensional particle mesh Ewald summation for the long-ranged interaction. To extract the excess fields $\Delta\boldsymbol{E}(z)$ and $\Delta\boldsymbol{D}(z)$, the corresponding fields at vanishing external field are subtracted. The SPC/E model is a nonpolarizable water model and therefore electronic polarization is not explicitly included in the model. However, electronic polarizability effects on molecular interactions are implicitly included via the parameterization of the Lennard-Jones term of the water model. The number density profiles at the two surface types are shown as solid lines in Fig. 1 (c)–(d). At the

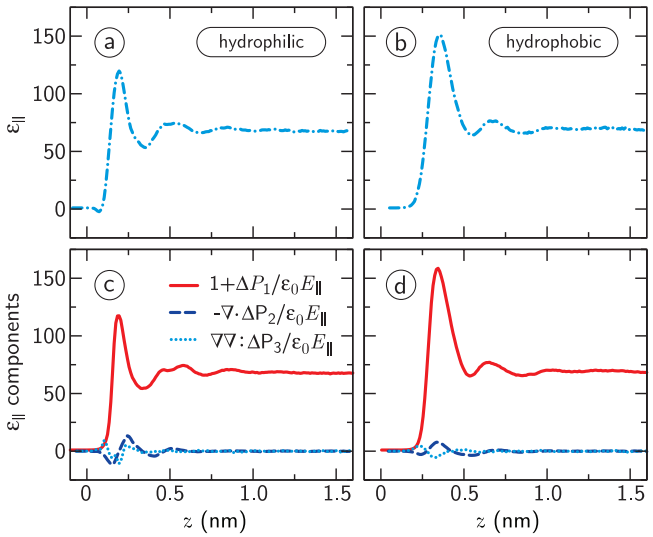

Figure 4: (a)–(b) Parallel dielectric response calculated from the explicit multipole expansion up to the octupole using Eq. 10 with Eqs. 11 & 17. The monopole and dipole (solid lines), quadrupole (dashed lines) and octupole (dotted lines) contributions are shown separately at (c) the hydrophilic and (d) the hydrophobic surface. All curves are calculated from the response to an applied electric field of $E_{\parallel} = 0.05$ V/nm using Eq. 25.

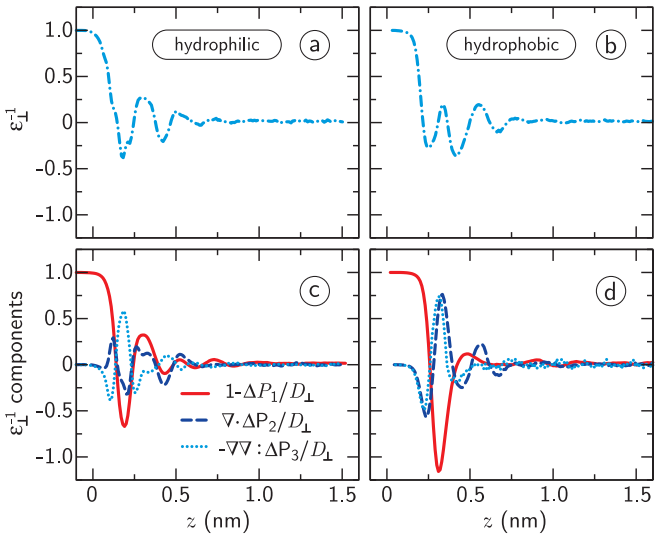

Figure 5: (a)–(b) Inverse perpendicular dielectric response calculated from the explicit multipole expansion up to the octupole using Eq. 10 with Eqs. 11 & 17. The monopole and dipole (solid lines), quadrupole (dashed lines) and octupole (dotted lines) contributions are shown separately at (c) the hydrophilic and (d) the hydrophobic surface. All curves are calculated from the average response to applied electric fields of $D_{\perp}/\varepsilon_0 = 2.0$, 4.0 and 8.0 V/nm using Eq. 27.

hydrophilic surface, the water molecules gather very close to the surface, whereas they form a depleted layer at the hydrophobic surface, conforming to previous results [37]. Most notably, the first peak of the water density at the hydrophilic surface is significantly higher than at the hydrophobic surface.

To examine the sensitivity of the results with respect to the water model used, we run two short simulations (5 ns) of the same surfaces in contact with TIP4P/2005 water [38], which has been shown to reproduce the experimental structure factor of water very well [39]. The density profiles of TIP4P/2005 are shown as dashed lines in Fig. 1 (c)–(d). Apart from a small discrepancy in the height of the first peak, the results are very similar to the results for SPC/E water. In particular, the minima and maxima of the density profiles coincide exactly. Although the quadrupole moment of TIP4P/2005 is $\sim$ 20% larger than that of SPC/E (in the isotropic phase, the xx, yy and zz components of $\bar{\mathsf{p}}_2$ equal 1.65 and $1.41 \times 10^{-3}\, e\,\mathrm{nm}^2$ for TIP4P/2005 and SPC/E, respectively, calculated with respect to the oxygen atom; the bar denotes averaging over all orientations), the dipole moments are almost identical (0.048 e nm for TIP4P/2005 and 0.049 e nm for SPC/E). Therefore, we expect the dielectric response of the two water models to be similar.

3.1 Dielectric Response

For the parallel orientation, either Cartesian direction x or y can be used. In the hydrophobic case, the diamond is perfectly isotropic, and the simulations give identical results in the x and y directions. In the hydrophilic case, however, there is a nonzero parallel polarization also in the absence of an electric field. This kind of ferroelectric behavior is due to the anisotropy of the OH-lattice on the surface. Since proportionality is assumed only for the excess quantities $\Delta\boldsymbol{E}$ and $\Delta\boldsymbol{D}$, the polarization at zero external field does not constitute a fundamental problem when using an applied external field. Nevertheless, problems may arise when using the fluctuation equation, because the fluctuation tensor may not be diagonal. Therefore, we diagonalize the fluctuation matrix, aligning the nonzero polarization at vanishing field in one direction. The diagonal fluctuation tensor contains the eigenvalues of the fluctuation tensor for each value of z. The largest eigenvalue corresponds to the direction tangentional to the surface in which $\langle\boldsymbol{M}\rangle_0 \neq 0$, the second-biggest to the surface tangentional direction in which $\langle\boldsymbol{M}\rangle_0 = 0$ and the smallest eigenvalue corresponds to the direction normal to the surface. In our analysis, we only use the second-largest eigenvalue of the fluctuation tensor, which to a good approximation is not affected by the nonzero polarization at vanishing field.

The resulting profiles of the parallel dielectric function are plotted in Fig. 2 for (a) the hydrophilic surface and (b) the hydrophobic surface, calculated using four different methods. For the first two methods, the polarization density $m_{\parallel}(z)$ is calculated from Eq. 35. The dashed lines result from an applied electric field of $E_{\parallel} = 0.05$ V/nm using Eq. 25 and the solid lines from the

fluctuations at vanishing electric field using Eq. 26. For both surface types, the profiles resulting from the fluctuation and applied field equations coincide excellently. For the second two methods, the polarization is estimated from the explicit expansion of Eq. 17 using terms up to the octupole moment. The multipole moments are calculated from Eqs. 10 & 11, where $\boldsymbol{r}_i$ is chosen to be the position of the oxygen atom. Again, the response is calculated from both an applied electric field using Eq. 25 (shown as dash-dotted lines) and from the polarization fluctuations using Eq. 26 (shown as dotted lines). The curves of the explicit expansion follow the curves of the full polarization, confirming the equivalence of the methods for calculating the polarization. The dielectric profile is roughly proportional to the number density, as would only be expected for noninteracting dilute polar particles. Surprisingly however, the first peak in the dielectric function at the hydrophobic surface is higher than at the hydrophilic surface, in opposite order of the peak heights of the density profiles in Fig. 1. This disparity indicates that, although there are more polarizable molecules available in the first density peak at the hydrophilic surface, their response to an electric field is more restricted than at the hydrophobic surface. Qualitatively, this result corresponds well to our notion that water is more strongly bound at hydrophilic surfaces. At the same time, it clearly shows that the simple picture of noninteracting dilute polar molecules is not sufficient to describe the dielectric profile of liquid water.

In Fig. 3, we show the inverse perpendicular dielectric function at (a) the hydrophilic surface and (b) the hydrophobic surface. Using the polarization $m_\perp(z)$ from Eq. 30, the response is calculated for an applied electric field of $D_\perp/\varepsilon_0 = 0.5$ V/nm (Eq. 27, dashed lines) and from the fluctuations (Eq. 28, solid lines). Like for the parallel response, the curves coincide, confirming our formalism and the validity of linear response theory for the applied field strength. Strikingly, $\varepsilon_\perp^{-1}(z)$ passes through zero several times, which means that $\varepsilon_\perp(z)$ has several singularities, and that there are spatial regions where the response is negative. This overscreening behavior is reminiscent of the nonlocal bulk dielectric function [10], which evidently dominates the perpendicular response. The excess electric field reaches zero where $\varepsilon_\perp^{-1}(z) = 0$ and reverses sign in the regions where $\varepsilon_\perp^{-1}(z) < 0$, giving rise to several local minima in the resulting electrostatic potential, as we will discuss in more detail in subsequent sections. In bulk, the inverse dielectric response corresponds to a bulk dielectric constant of $\varepsilon_{\text{bulk}} = 75$, which is close to the literature value for SPC/E water of 71 [40]. Also shown in Fig. 3 are the curves calculated from the explicit expansion of Eq. 17 up to the octupole moment, showing a satisfactory agreement with the response of the full polarization, like in the parallel case.

► **Multipole components.** As the similarity of the curves in Figs. 2 and 3 distinctly show, the first three terms of the multipole expansion of Eq. 17 suffice to describe the dielectric tensor. To compare the contributions of the individual multipole moments, we show the first three terms separately. First, the sum of the first three terms of the parallel response is shown in Fig. 4 at (a) the hydrophilic surface and (b) the hydrophobic surface. Second, we show the corresponding components separately in Fig. 4 (c)–(d). Quadrupole and octupole contributions show similar profiles at the two surface types, but clearly, the dipole contribution dominates the parallel response. In Fig. 5 (a)–(b), we show the sum of the first three contributions to the perpendicular response, and the separate terms in (c)–(d). Contrary to the parallel case, the higher-order terms are non-negligible. In fact, the effect of the dipole is largely compensated for by the higher-order terms at both surface types. This clearly illustrates the importance of the higher-order electric multipoles for the perpendicular dielectric response.

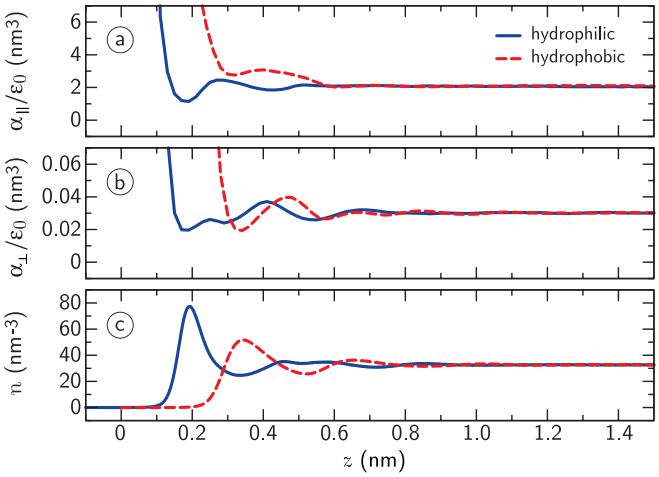

Figure 6: Polarizability as a function of z calculated from Eq. 36 in (a) parallel direction and (b) perpendicular direction. Due to the nonpolarizable water model used, the polarizability only includes multipole orientational effects. The number density is plotted in panel (c) for comparison.

► **Polarizability.** For a dilute system of noninteracting particles, the dielectric function can be written as $1+\alpha n(\boldsymbol{r})/\varepsilon_0$, with $n(\boldsymbol{r})$ the number density of dielectric molecules and α a microscopic polarizability attributed to each individual water molecule [34]. To describe the dielectric constant in condensed media, corrections to the polarizability appear, as in the famous Clausius-Mosotti expression. To quantify the deviation from the predicted response of a dilute system of noninteracting polar particles, we calculate the space-dependent polarizability, defined according to linear theory as

$$\frac{\alpha_\parallel(z)}{\varepsilon_0} = \frac{\varepsilon_\parallel(z)-1}{n(z)} \quad \text{and} \quad \frac{\alpha_\perp(z)}{\varepsilon_0} = \frac{1-\varepsilon_\perp^{-1}(z)}{n(z)}. \tag{36}$$

Clearly, because the dielectric profile is calculated using a nonpolarizable water model, the polarizability $\alpha(\boldsymbol{r})$ does not explicitly include electronic, but only orientational

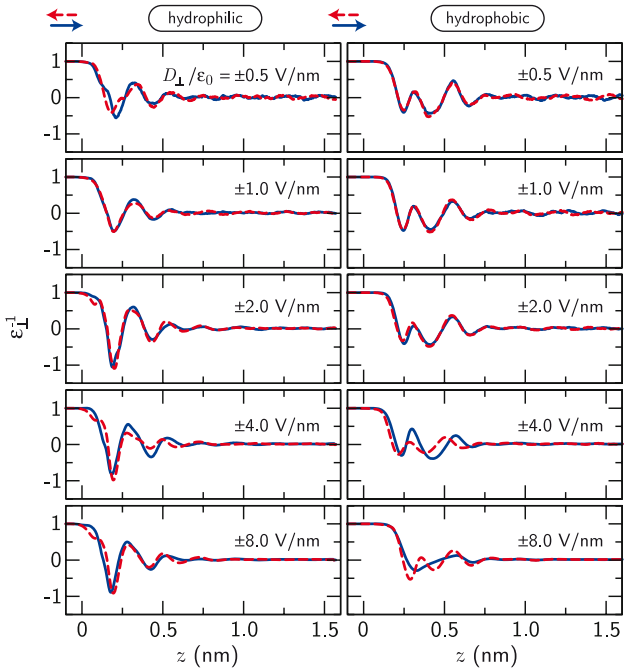

Figure 7: The inverse perpendicular dielectric response function $\varepsilon_\perp^{-1}(z)$ calculated from Eq. 27 at different values of the external field strength $D_\perp$. The position $z = 0$ corresponds to the oxygen layer at the hydrophilic surface and the outermost carbon layer at the hydrophobic surface.

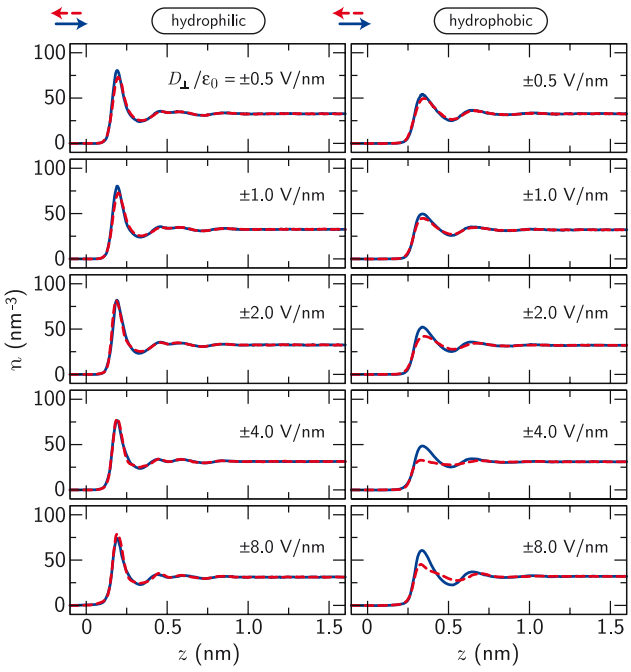

Figure 8: The molecular number density $n(z)$ at different values of the perpendicular external field strength $D_\perp/\varepsilon_0$.

polarization. The main question is whether the polarizability exhibits any simple relation with the particle density. Both polarizabilities are plotted in Fig. 6 (a)–(b) as a function of z, together with the number density (c). In both the parallel and perpendicular directions and at both surface types, the polarizability exhibits a dip at the position of the highest density. Another prominent feature is that the parallel polarizability at the hydrophobic surface is always higher than in bulk, whereas the parallel polarizability decreases at the hydrophilic surface. Overall, the curves show that the relation between the different components of the polarizability and the particle density is intricate and depends on surface type.

► **Beyond linear response.** In Fig. 7, the perpendicular component of the inverse dielectric constant (Eq. 27) is plotted as a function of z for different values of the external electric field strength $D_\perp/\varepsilon_0$. Apart from a slight difference between the curves taken at constant pressure (up to 1 V/nm) and constant volume, the response at the hydrophilic interface is largely independent of the applied field strength. At the hydrophobic interface, however, the dielectric response is clearly nonlinear at external field strengths of 4.0 V/nm and above, as can be seen from the different response to the different field directions. At a positive electric field of 8.0 V/nm, the overscreening seems to be slightly suppressed, as is commonly found in ionic liquids at high electric field strength [41, 42]. Thus, the linear response regime extends to higher field strengths at the hydrophilic interface. It should be noted that the curves in Fig. 7 are calculated using a nonpolarizable water model, and therefore do not include electronic polarization or ionization effects. Experimental results indicate that on timescales of 0.01–10 μs the dielectric breakdown of water occurs at a field strength of the order of ~ 0.1 V/nm [43]. That means that the nonlinear response due to multipole orientational effects shown in Fig. 7 is not expected to play a role in the nonlinear response of real water. We plot the corresponding density profiles in Fig. 8. Similar to the dielectric profile, the density profile at the hydrophilic interface is independent of the external field strength, whereas the density at the hydrophobic interface gradually changes with increasing electric field strength. The nonlinear response at high electric field strength has a minor, but distinct influence on the effective dielectric properties of the interface, as we will discuss in the context of the effective dielectric interface position in the section on coarse-grained modeling approaches.

3.2 Other Effects of the Higher-Order Multipole Moments on Interfacial Electrostatics

The strong effect of the higher-order electric multipole moments on the interfacial water structure manifests itself not only in the dielectric response but also in the electric field in the interfacial region in absence of an applied external electric field and consequently in the

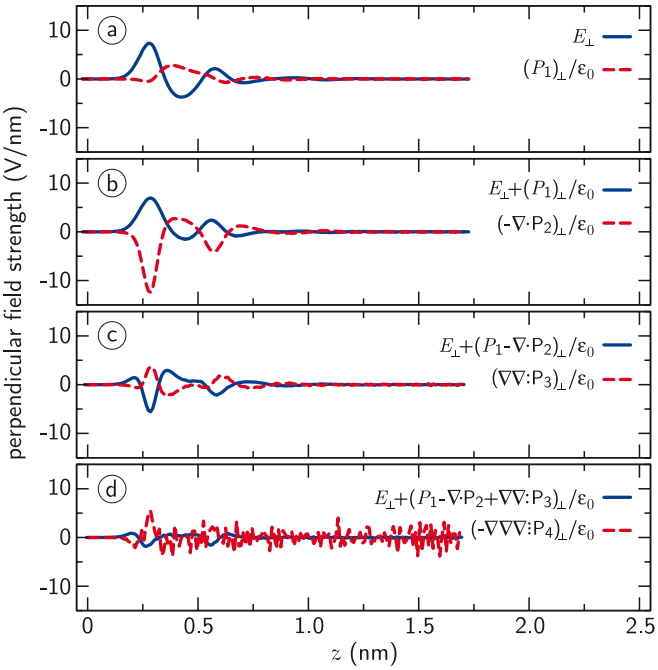

Figure 9: The perpendicular components of the terms of the multipole expansion given in Eqs. 15 and 17, summing the terms to increasing order. The profiles correspond to the hydrophobic diamond surface without external displacement field. The electric field $E_\perp(z)$ is calculated from Eq. 29 and higher-order terms from Eqs. 10 & 11. The molecular multipole moments are calculated with respect to the oxygen atom.

potential difference across an aqueous interface. For instance, this surface potential difference is important for the calculation of single ion solvation free energies.

► **The perpendicular displacement field.** In the absence of free charges, the displacement field perpendicular to the interface is constant in space. When the expansion of the displacement field is truncated after the dipole term, however, the resulting sum is certainly not constant. An illustration is provided in Fig. 9, where we plot the perpendicular components of the terms of Eqs. 15 and 17, summing to increasing order for the case of vanishing displacement field. As can be seen in Fig. 9 (b), the sum $\boldsymbol{E}+\boldsymbol{P}_1/\varepsilon_0$ varies appreciably across the interface, but the variation is largely compensated for by the quadrupole term $-\nabla\cdot\mathsf{P}_2/\varepsilon_0$. The remaining oscillations are again almost fully compensated for by the octupole term $\nabla\nabla:\mathsf{P}_3/\varepsilon_0$ shown in Fig. 9 (c). The oscillations of the hexadecapole term drop below the noise level, see Fig. 9 (d). Evidently, the higher-order multipole moments, at least up to the octupole term, are critical to describing the electrostatics at the interface properly.

► **Surface potential of aqueous interfaces.** The value of the electrostatic potential difference across an air-water interface has been a source of confusion for decades, with people not even agreeing on its sign, see Ref. [44] for a review. Experimental evidence indicates that the water molecules are preferentially oriented with the dipole moment pointing roughly along the surface plane at air-water interfaces [45] and at quarz-water interfaces [46, 47], leaving the question of the sign of the dipole contribution open. It is well-known however, that the quadrupole contribution to the interface potential cannot be ignored [23, 48, 49]. We calculate the interface potential of the water-diamond surface, split into the dipole and quadrupole contributions. The potential profile across the interfacial layer is given by

$$\psi(z)-\psi(z_s)=-\int_{z_s}^{z}E_\perp(z')\,\mathrm{d}z'. \tag{37}$$

with z_s being a reference position in the solid phase. In the following calculations, we choose $\psi(z_s)=0$. In case of a charge-free interface without external electric field, inserting Eqs. 15 and 17 produces

$$\psi(z)=\int_{z_s}^{z}\frac{\boldsymbol{P}_1^z(z')}{\varepsilon_0}\,\mathrm{d}z'-\int_{z_s}^{z}\frac{\mathrm{d}\mathsf{P}_2^{zz}(z')}{\mathrm{d}z'\varepsilon_0}\,\mathrm{d}z', \tag{38}$$

where $\boldsymbol{P}_1^z(z)$ denotes the z component of the dipole density and $\mathsf{P}_2^{zz}(z)$ denotes the zz component of the quadrupole density. Higher-order moments do not contribute, because integrals over the corresponding fields yield the boundary values of derivatives of the multipole densities, which vanish because of the constant value of any multipole density both in the charge-free solid and in the bulk. When integrated across the entire interfacial layer, the second term of Eq. 38 yields the negative difference between the quadrupole density in the bulk liquid and solid phase,

$$-\int_{z_s}^{z_l}\frac{\mathrm{d}\mathsf{P}_2^{zz}(z')}{\mathrm{d}z'\varepsilon_0}\,\mathrm{d}z'=\frac{\mathsf{P}_2^{zz}(z_s)-\mathsf{P}_2^{zz}(z_l)}{\varepsilon_0}=-\frac{\bar{\mathsf{P}}_2^{zz}}{\varepsilon_0}, \tag{39}$$

with z_l being a position in the bulk liquid phase. The bar denotes the value in the isotropic phase. The quadrupole moment of a SPC/E water molecule in the isotropic phase is calculated by isotropic angular averaging, giving $\bar{\mathsf{p}}_2=1.41\times10^{-3}\,e\,\mathrm{nm}^2$. To obtain the quadrupole density $\bar{\mathsf{P}}_2/\varepsilon_0$ in volts, the molecular quadrupole moment is multiplied by the bulk water number density $n_{\mathrm{bulk}}=33\ \mathrm{nm}^{-3}$ and divided by ε_0, yielding

$$\frac{\bar{\mathsf{P}}_2}{\varepsilon_0}=\begin{bmatrix}0.8428&0&0\\0&0.8428&0\\0&0&0.8428\end{bmatrix}\mathrm{V}. \tag{40}$$

In Fig. 10, the potential profile across the interface, calculated from simulations of the hydrophobic diamond in water, is plotted as a function of the perpendicular coordinate z. The solid dark-blue line indicates the profile as calculated from Eq. 37, giving a potential difference of −0.44 V between bulk liquid and solid. Taking only the dipole contribution into account yields 0.40 V (red

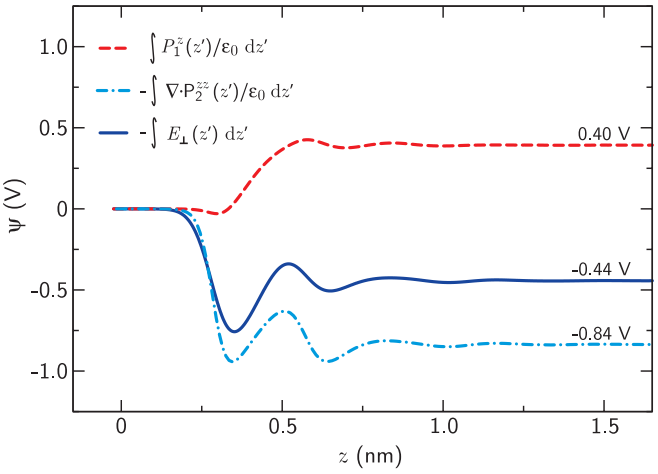

Figure 10: The electrostatic potential profile across a charge-free hydrophobic diamond-water interface calculated from the electric field (Eq. 37, solid line) and split into the two components of Eq. 38: the dipole contribution (dashed line) and the quadrupole contribution (dash-dotted line). The potential is calculated with respect to the reference electrostatic potential in the solid phase.

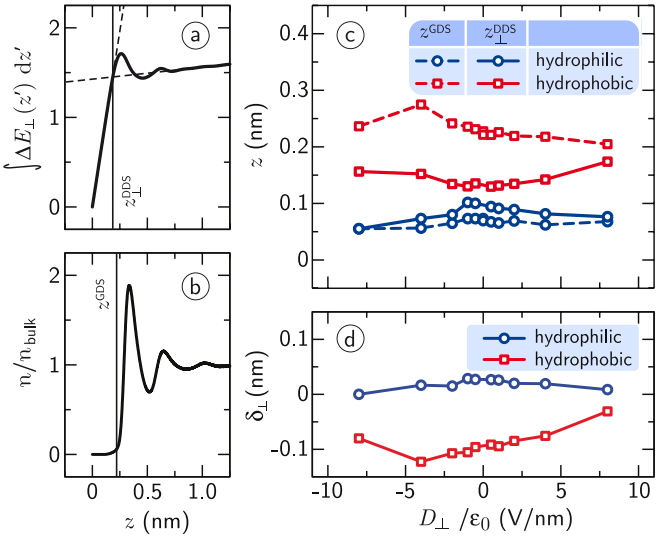

Figure 11: (a) Graphical representation of the construction of the perpendicular dielectric dividing surface $z_\perp^{\mathrm{DDS}}$ by extrapolation of the bulk potential profile (Eq. 42, where $\Delta E_\perp$ is calculated from Eq. 29 in separate simulations with and without external displacement field). The curve shown corresponds to an external displacement field of $D_\perp/\varepsilon_0 = 8.0$ V/nm. (b) The corresponding Gibbs dividing surface z^{GDS}. (c) Positions of the perpendicular dielectric dividing surface $z_\perp^{\mathrm{DDS}}$ and the Gibbs dividing surface z^{GDS} as a function of the applied perpendicular electric field. (d) The perpendicular dielectric interface shift $\delta_\perp = z_\perp^{\mathrm{DDS}} - z^{\mathrm{GDS}}$ as a function of the applied perpendicular electric field.

dashed line in Fig. 10), which has the opposite sign. The voltage drop is restored to the correct value upon addition of the quadrupole contribution (dash-dotted light-blue line), which equals the value calculated from averaging the quadrupole moment of the SPC/E water model over all orientations (Eq. 40). Although the molecular dipole moment does not depend on the choice of origin, both the dipole and quadrupole density depend on the reference point chosen for the expansion. For water there is no choice of origin for which either one vanishes. Therefore, both contributions are important for the total interface potential, but the relative values of the dipolar and quadrupolar contributions vary depending on the choice of origin.

4 Coarse-Grained Modeling

► **Dielectric dividing surface.** Instead of the profile of the inverse dielectric response function begin used, the dielectric profile at an interface can be modeled by a sharp discontinuity, but shifted with respect to the Gibbs dividing surface. The Gibbs dividing surface, which is the thermodynamically defined interface position, is calculated as usual,

$$z^{\mathrm{GDS}} = z_s - \int_{z_s}^{z_l} \frac{n(z_l) - n(z)}{n(z_l) - n(z_s)}\,\mathrm{d}z, \qquad (41)$$

with $n(z)$ being the water density and z_l and z_s being positions in the bulk liquid and solid phase, respectively. Equivalent to Eq. 41, we introduce the dielectric dividing surface,

$$z^{\mathrm{DDS}} = z_s + \int_{z_s}^{z_l} \frac{f(z_l) - f(z)}{f(z_l) - f(z_s)}\,\mathrm{d}z. \qquad (42)$$

For the parallel dielectric dividing surface we take $f(z) = \varepsilon_\parallel(z)$, while for the perpendicular dielectric dividing surface we take $f(z) = \varepsilon_\perp^{-1}(z)$. The values of z^{GDS}, $z_\parallel^{\mathrm{DDS}}$ and $z_\perp^{\mathrm{DDS}}$ at vanishing external field are summarized in Tab. 1. The Gibbs dividing surface position clearly shows that water at the hydrophilic surface moves close to the interface, whereas water retreats from the hydrophobic surface. However, this difference in depletion layer hardly manifests itself in the position of the dielectric dividing surface, which is similar for both surface types. To quantify the difference between the two surface types, we look at the dielectric interface shift $\delta = z^{\mathrm{DDS}} - z^{\mathrm{GDS}}$. From Tab. 1 it follows $\delta_\perp^{\mathrm{phob}} = -0.10$ nm and $\delta_\parallel^{\mathrm{phob}} = -0.14$ nm at the hydrophobic surface and $\delta_\perp^{\mathrm{phil}} = 0.03$ nm and $\delta_\parallel^{\mathrm{phil}} = 0.02$ nm at the hydrophilic surface. Interestingly, the difference in parallel and perpendicular dielectric interface shift is relatively small, whereas the different surface types actually give rise to shifts of opposite sign. This remarkable difference in the dielectric interface shift signifies that water at the hydrophobic surface is a "better dielectric" than at the hydrophilic surface. For the perpendicular profile, the width of the dielec-

tric variation has been defined earlier in a similar way [7, 8]. The difference between the two definitions is that $z_\perp^{\mathrm{DDS}}$ as defined in Eq. 42 guarantees that the electrostatic potential far away from the interface is correctly reproduced. This can be seen by realizing that $z_\perp^{\mathrm{DDS}}$ corresponds to the position where the extrapolated linear fits to the solid and bulk liquid potential profile cross each other, see Fig. 11 (a). Using $\nabla\psi(z) = -E_\perp(z)$ and Eqs. 4 and 42, the electrostatic potential difference between liquid and solid is given by

$$\begin{aligned}\psi(z_l) - \psi(z_s) &= -\frac{D_\perp}{\varepsilon_0}\int_{z_s}^{z_l} \varepsilon_\perp^{-1}(z)\,\mathrm{d}z \\ &= -\frac{D_\perp}{\varepsilon_0}\left(\int_{z_s}^{z_\perp^{\mathrm{DDS}}} \mathrm{d}z + \int_{z_\perp^{\mathrm{DDS}}}^{z_l} \frac{\mathrm{d}z}{\varepsilon_{\mathrm{bulk}}}\right),\end{aligned} \tag{43}$$

for a constant displacement field $D_\perp$. Therefore, using a sharp-kink approximation of the dielectric profile,

$$\varepsilon_\perp(z) = \begin{cases} 1 & \text{if } z < z_\perp^{\mathrm{DDS}} \\ \varepsilon_{\mathrm{bulk}} & \text{otherwise,} \end{cases} \tag{44}$$

ensures the correct asymptotic voltage profile far away from the interface. To compare the dielectric interface position with the Gibbs dividing surface, the density profile and the Gibbs dividing surface z^{GDS} are shown in Fig. 11 (b). In Fig. 11 (c), we show the positions of z^{GDS} and $z_\perp^{\mathrm{DDS}}$, showing a mild dependence on the external displacement field strength. For all values of the external displacement field, the dielectric dividing surface is located close to the Gibbs dividing surface at the hydrophilic surface, displaced slightly into the fluid, whereas at the hydrophobic surface, the dielectric interface is shifted towards the solid surface. The perpendicular dielectric interface shift, defined as $\delta_\perp = z_\perp^{\mathrm{DDS}} - z^{\mathrm{GDS}}$, is shown in Fig. 11 (d). At the hydrophilic surface, the dielectric interface shift slightly declines at high external field strength, which means that the water becomes a slightly better dielectric. At the hydrophobic surface, however, the dielectric interface shift not only depends on the applied field strength, but also on the field direction, in line with our results for the dielectric profiles.

Table 1: Dielectric and Gibbs dividing surfaces of the two different surface types measured with respect to the positions of the outermost heavy atoms.[a]

Surface type	z^{GDS} (nm)	$z_\parallel^{\mathrm{DDS}}$ (nm)	$z_\perp^{\mathrm{DDS}}$ (nm)
Hydrophilic	0.07	0.09	0.10
Hydrophobic	0.22	0.08	0.12

[a] *I.e.* the oxygen atoms of the hydroxyl groups at the hydrophilic surface and the carbon atoms at the hydrophobic surface.

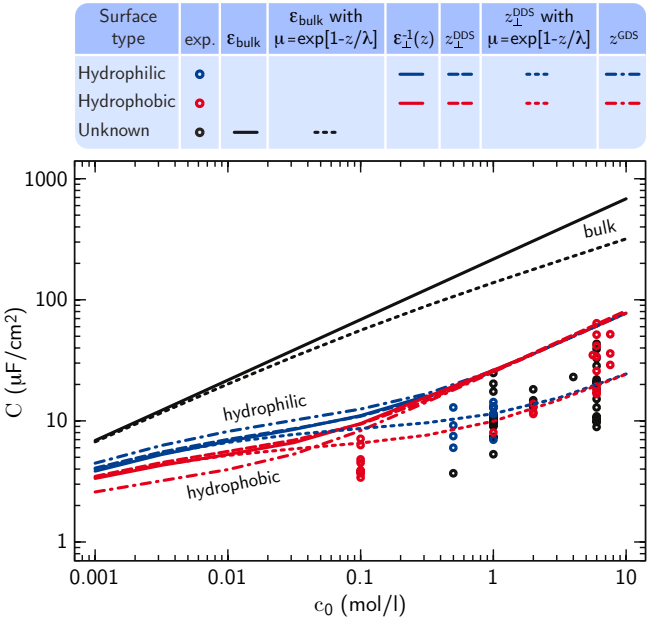

Figure 13: Capacitance of the double layer, from Eq. 52 and the solution to the Debye-Hückel equation (Eq. 53). The black lines are calculated assuming bulk permittivity in the entire fluid and $\mu(z) = 0$ (solid line) or $\mu(z) = \exp[1 - z/\lambda]$ (dotted line). The blue lines (hydrophilic) and red lines (hydrophobic) are calculated using different approximations for the dielectric properties: the full profile $\varepsilon_\perp^{-1}(z)$ or the sharp-kink approximation of Eq. 44 at either the dielectric dividing surface $z_\perp^{\mathrm{DDS}}$ or the Gibbs dividing surface z^{GDS}.

The trend as a function of field strength, however, is to increase $\delta_\perp^{\mathrm{phob}}$, which means that the dielectric becomes slightly worse.

► **Poisson-Boltzmann equation.** We consider a charged planar surface with monovalent counterions, where the charge density is laterally averaged and only depends on the z direction. For a charged surface with counterions in solution neither $\boldsymbol{E}(z)$ nor $\boldsymbol{D}(z)$ is constant, so the integral of Eq. 3 does not yield a local dielectric function automatically. Therefore, inspired by Eq. 4, we assume

$$\varepsilon_0 E_\perp(z) = \varepsilon_\perp^{-1}(z)\, D_\perp(z), \tag{45}$$

which is a good approximation when $D_\perp(z)$ varies slowly, *i.e.* at low salt concentration and at low surface charge density. Taking the divergence of Eq. 45 and using $\nabla\psi(z) = -E_\perp(z)$ leads to

$$\varepsilon_0 \frac{\mathrm{d}^2\psi}{\mathrm{d}z^2} = -D_\perp(z)\frac{\mathrm{d}\varepsilon_\perp^{-1}}{\mathrm{d}z} - \varepsilon_\perp^{-1}(z)\frac{\mathrm{d}D_\perp}{\mathrm{d}z}. \tag{46}$$

Inserting the Boltzmann expression for the ion density,

$$\frac{\mathrm{d}D_\perp}{\mathrm{d}z} = P_0(z) = -2ec_0 \sinh[-\beta e\psi(z)] \exp[-\mu(z)], \tag{47}$$

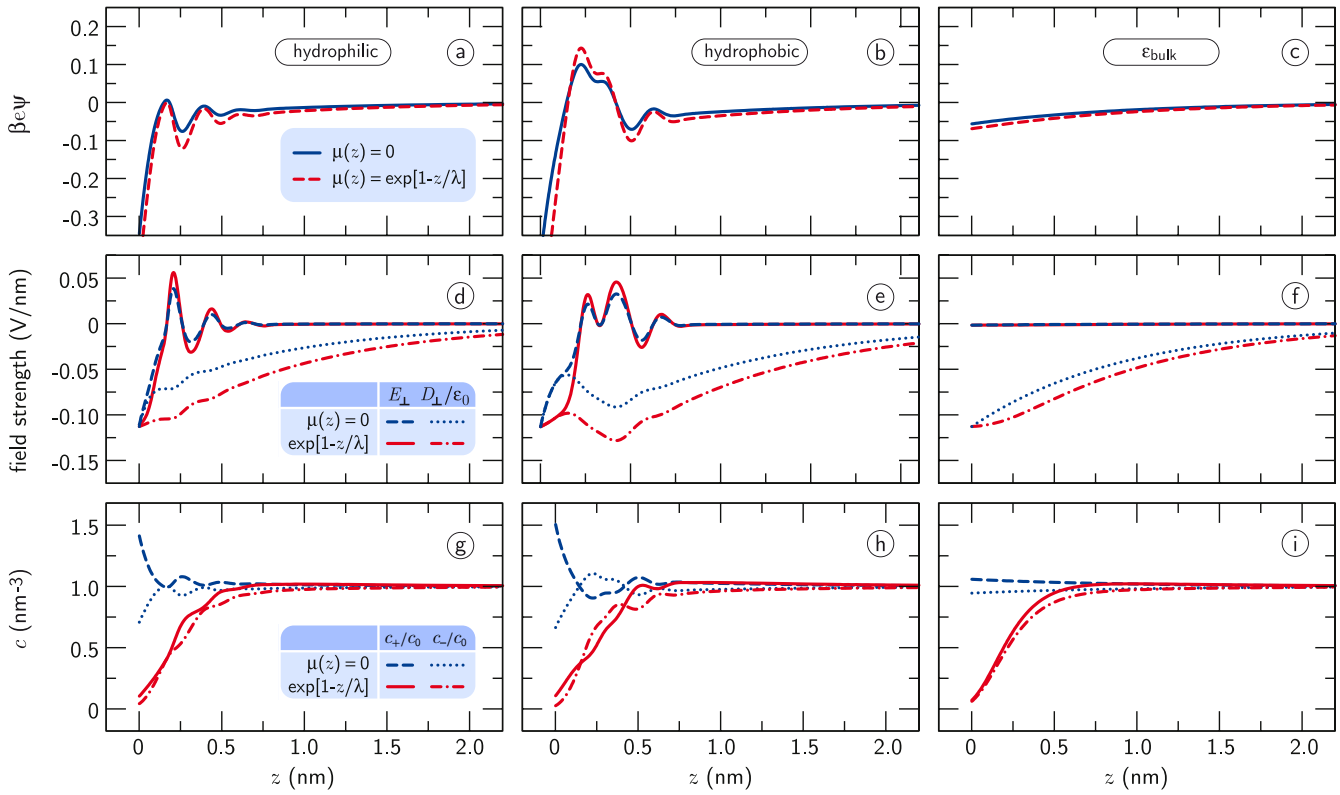

Figure 12: (a)–(c) The electrostatic potential next to a charged surface ($\sigma_0 = -0.006\ e/\mathrm{nm}^2$), calculated from the Poisson-Boltzmann equation (Eq. 48) and different models of the dielectric function $\varepsilon_\perp^{-1}(z)$. Curves are shown for the hydrophilic profile (left), the hydrophobic profile (middle), and $\varepsilon_\perp^{-1}(z) = \varepsilon_{\mathrm{bulk}}^{-1}$ (right). The bulk salt concentration is $c_0 = 100$ mM. (d)–(f) The perpendicular electric field $E_\perp(z)$ and the perpendicular displacement field $D_\perp(z)/\varepsilon_0$. (g)–(i) The corresponding ionic density profiles c_+ (positive ions, solid lines) and c_- (negative ions, dashed lines), normalized on the bulk density c_0. We have used either no nonelectrostatic potential ($\mu(z) = 0$) or the repulsive potential of Eq. 51 ($\mu(z) = \exp[1 - z/\lambda]$ with $\lambda = 0.15$ nm).

with c_0 the ionic concentration in bulk, we arrive at the modified Poisson-Boltzmann equation,

$$\varepsilon_0 \frac{\mathrm{d}^2\psi}{\mathrm{d}z^2} = -D_\perp(z)\frac{\mathrm{d}\varepsilon_\perp^{-1}}{\mathrm{d}z} + 2ec_0 \sinh[-\beta e\psi(z)] \exp[-\mu(z)]\, \varepsilon_\perp^{-1}(z). \quad (48)$$

The potential $\mu(z)$ contains all nonelectrostatic contributions from the interface, such as steric and solvophobic effects. The displacement field in the first term of Eq. 48 is calculated from

$$D_\perp(z) = \int_0^z P_0(z')\,\mathrm{d}z', \quad (49)$$

making Eq. 48 a second-order integro-differential equation. Eqs. 47–49 are solved numerically, imposing a fixed surface charge density σ_0 as a boundary condition at $z = 0$. The position $z = 0$ corresponds to the oxygen atoms at the hydrophilic surface and to the outermost carbon atom at the hydrophobic surface.

► **Electrostatic potential.** We calculate the electrostatic potential close to a surface carrying a minute surface charge density $\sigma_0 = -0.006\ e/\mathrm{nm}^2$ (-1 mC/m^2) at a salt concentration of 100 mM (0.1 mol/l). The effect that the finite salt concentration may have on the dielectric profile $\varepsilon_\perp(z)$ can be expressed in terms of the ionic excess polarizabilities $\Delta\alpha_\pm$,

$$\varepsilon_\perp(z) = \varepsilon_{\perp,\mathrm{H_2O}}(z) + \frac{c_+(z)\,\Delta\alpha_+}{\varepsilon_0} + \frac{c_-(z)\,\Delta\alpha_-}{\varepsilon_0}, \quad (50)$$

with $\varepsilon_{\perp,\mathrm{H_2O}}(z)$ the pure water profile that we have calculated. In the following we set $\Delta\alpha_\pm = 0$, which means that any effect that the finite salt concentration may have on the profile $\varepsilon_\perp^{-1}(z)$ is ignored. The electrostatic potential is shown in Fig. 12 (a)–(c) for two different choices of $\mu(z)$: without a nonelectrostatic interaction, $\mu(z) = 0$, and including a generic soft-wall repulsion, modeled by

$$\mu(z) = \gamma \exp[1 - z/\lambda], \quad (51)$$

with λ being the size of a typical ionic radius, $\lambda = 0.15$ nm and $\gamma = 1$. Strikingly, the electrostatic potential at the hydrophobic interface changes sign between 0.2 and 0.4 nm from the wall, locally enhancing the concentration of co-ions. This means that, locally, the charge on the surface is overscreened by the sum of polarization and

ionic charges, a phenomenon that is well known to occur in ionic liquids as well [42]. In Fig. 12 (d)–(f) we plot the corresponding perpendicular electric field $E_\perp(z)$ and the perpendicular displacement field $D_\perp(z)/\varepsilon_0$. Importantly, the displacement field $D_\perp(z)$ varies more slowly than the electric field $E_\perp(z)$, which justifies the use of the local approximation of Eq. 45. The ionic densities $c_\pm(z) = c_0 \exp[\mp\beta e\psi(z) - \mu(z)]$ are plotted in Fig. 12 (g)–(i), clearly showing the effect of overscreening at the hydrophobic surface. Remarkably, when the dielectric profile is used instead of $\varepsilon_{\text{bulk}}$, the ions accumulate closer to the surface. The soft-wall repulsion, however, pushes the ions away from the surface, although its effect on the electrostatic potential profile is minor. That means that in cases where the nonelectrostatic repulsion is less pronounced, we expect the counterions to be strongly bound to the surface because of dielectric effects.

► **Capacitance of the double layer.** The double-layer structure of the charged interface and its counterion cloud gives rise to a capacitance. The vast amount of experimental data on interfacial capacitances provides a direct test of the model for the dielectric profile. Because the point of vanishing surface potential $\psi_0 = \psi(0)$ is hard to determine and because the capacitance may depend on the surface potential, the differential capacitance is generally reported,

$$C = \frac{\mathrm{d}\sigma_0}{\mathrm{d}\psi_0}. \tag{52}$$

We calculate the differential capacitance of a Poisson-Boltzmann distribution of ions next to a charged surface, comparing the models for the dielectric profile discussed above. Using the nonlinear Poisson-Boltzmann equation, the differential capacitance depends on the surface charge density, but using the Debye-Hückel approximation, the differential capacitance is constant and equal to the capacitance from the nonlinear Poisson-Boltzmann equation in the limit $\sigma_0 \to 0$. The Debye-Hückel limit is obtained by approximating Eq. 48 for small $\psi(z)$,

$$\varepsilon_0 \frac{\mathrm{d}^2\psi}{\mathrm{d}z^2} = -D_\perp(z)\frac{\mathrm{d}\varepsilon_\perp^{-1}}{\mathrm{d}z} - 2ec_0\beta e\psi(z)\exp[-\mu(z)]\varepsilon_\perp^{-1}(z), \tag{53}$$

which has to be solved together with Eq. 49. In Fig. 13, we show the double-layer capacitance using the different models for the interfacial dielectric properties discussed above, comparing the results to experimental data. The blue circles in Fig. 13 denote experimental data on surfaces that are known to be hydrophilic (contact angle below 90°), the red circles denote data on hydrophobic surfaces, and the black circles denote data on surfaces of which the contact angle is unknown. The electrolytes used in the experiments are sulfuric acid (H_2SO_4) and potassium hydroxide (KOH). Further details and references are listed in the Appendix. As a first model, we show the differential capacitance of Eq. 52 as a function of salt concentration c_0 using a dielectric constant equal to $\varepsilon_{\text{bulk}}$ and $\mu(z) = 0$ (black solid line), which overestimates the experimental data by at least an oder of magnitude. This discrepancy led Stern to propose a model where a thin layer at the interface has a lower dielectric constant than the bulk fluid [13]. Second, we include the generic soft-wall repulsion given in Eq. 51, with $\lambda = 0.15$ nm and $\gamma = 1$. The capacitance, shown as a black dotted line, captures neither the trend nor the magnitude of the experimental data much better. Third, we use our calculated full dielectric profile $\varepsilon_\perp^{-1}(z)$ (shown in Fig. 3) with $\mu(z) = 0$ (solid colored lines), agreeing much better with experiments. The hydrophilic profile (blue) yields a slightly higher capacitance than the hydrophobic profile (red) for low salt concentration, which is generally expected because of the better wetting characteristics [50]. The difference is minor, however, because the dielectric interface shift $\delta_\perp$ largely compensates for the depletion gap at hydrophobic surfaces. Fourth, we use the sharp-kink approximation of Eq. 44 with $\mu(z) = 0$ (dashed colored lines). The results are almost indistinguishable from the curves calculated using the full profiles $\varepsilon_\perp^{-1}(z)$, as expected from the fact that the dielectric dividing surface is designed to reproduce the electrostatic potential far away from the interface. Nevertheless, the calculated capacitance is still relatively high compared to the experimental data, which has to do with the fact that in the Poisson-Boltzmann approach the point-charge ions are allowed to get arbitrarily close to the surface. Therefore, as a fifth model, we use the sharp-kink approximation of Eq. 44 together with $\mu(z)$ from Eq. 51, shown as dotted colored lines. Clearly, this model follows the experimental data very well. Values of the calculated capacitance can be adjusted by fine-tuning the parameters γ and λ, which are expected to depend on the surface and ion type. Finally, we show the capacitance using a sharp-kink approximation for $\varepsilon_\perp^{-1}(z)$ located at z^{GDS} (dash-dotted lines), which does not perform as well as the sharp-kink approximation located at $z_\perp^{\text{DDS}}$. In fact, using the Gibbs dividing surface, the difference between hydrophilic and hydrophobic surfaces is quite large for low salt concentration, which does not seem to be reflected in the experimental data. Turning this argument around, the approximate equality of experimental data for the double-layer capacitance on hydrophilic and hydrophobic surfaces displayed in Fig. 13 can be viewed as a confirmation of one of the main results of the present work, namely that the effect of the depletion layer at hydrophobic surfaces is largely compensated for by the dielectric properties of the first few interfacial water layers, effectively yielding dielectric properties similar to those at hydrophilic surfaces.

► **Effective Stern layer permittivity.** Within the original Stern model of a charge-free interfacial region of width d with dielectric constant ε_{int}, the capacitance turns out to be $C_{\text{Stern}} = \sigma_0/\psi_0 = \varepsilon_{\text{int}}\varepsilon_0/d$. The same model yields $C_{\text{bulk}} = \varepsilon_{\text{bulk}}\varepsilon_0/d$ when the bulk value

$\varepsilon = \varepsilon_{\rm bulk}$ is assumed for the interfacial dielectric constant. Therefore the capacitance ratio reflects the ratio of interfacial dielectric constants,

$$\frac{C_{\rm Stern}}{C_{\rm bulk}} = \frac{\varepsilon_{\rm int}}{\varepsilon_{\rm bulk}}. \qquad (54)$$

By imposing Eq. 54 and dividing the capacitance which follows from the solution of the Poisson-Boltzmann equation including the dielectric profile $\varepsilon_\perp^{-1}(z)$ by the capacitance using the bulk assumption $\varepsilon_\perp^{-1}(z) = \varepsilon_{\rm bulk}^{-1}$, the estimate for $\varepsilon_{\rm int}$ varies between 10 and 30, depending on salt concentration, which corresponds well to earlier estimates based on experimental data [11, 12]. Our results present a microscopic picture of the electrostatic properties of the interfacial layer, allowing for the analysis of not only the double-layer capacitance, but also other properties, such as the electrostatic pressure between two plates as a function of separation, as will be detailed next.

► **Disjoining pressure between charged plates.** We determine the disjoining pressure between two plates from the free energy $\mathcal{F}$ calculated using the Poisson-Boltzmann equation [51, 11, 52, 53],

$$\beta\mathcal{F} = \beta\sigma_0\psi_0 + \int \frac{\beta\psi(z)}{2} P_0(z) + \sum_\pm c_\pm(z)\left[\mu(z) + \ln\frac{c_\pm(z)}{c_0} - 1\right] {\rm d}z, \qquad (55)$$

with σ_0 being the surface charge density, $\psi_0 = \psi(0)$ the potential at the wall and $c_\pm(z) = c_0 \exp[\mp\beta e\psi(z) - \mu(z)]$ being the ionic densities. The potential $\psi(z)$ is calculated from the nonlinear Poisson-Boltzmann equation given in Eq. 48. The first term in Eq. 55 comes from the surface integral over the electrostatic energy of the surface charge density. The pressure $p(d)$ between two plates at separation d is given by

$$\beta\, p(d) = -\frac{{\rm d}\beta\mathcal{F}}{{\rm d}d} - 2c_0. \qquad (56)$$

For the dielectric profile between the two plates, we join the $\varepsilon_\perp^{-1}(z)$ profiles from both surfaces piecewise together. The resulting pressure is shown in Fig. 14 for a 100 mM monovalent salt solution and a surface charge of $-0.006\ e\ {\rm nm}^{-2}$ ($-1\ {\rm mC/m^2}$). Compared to a spatially constant bulk dielectric function (black solid line), the pressure is lower when the full dielectric profile $\varepsilon_\perp^{-1}(z)$ (solid colored lines) or the sharp-kink approximation of Eq. 44 (colored dashed lines) is used. Therefore, modifications of the pressure between charged surfaces due to dielectric surface effects cannot explain, and probably are also not related to, the exponentially decaying short-ranged hydration repulsion, which is found experimentally and theoretically between all kinds of polar surfaces [30, 54]. On the basis of a mean-field type interpretation (without taking the dielectric profile into account) of pressures obtained within atomistic simulations

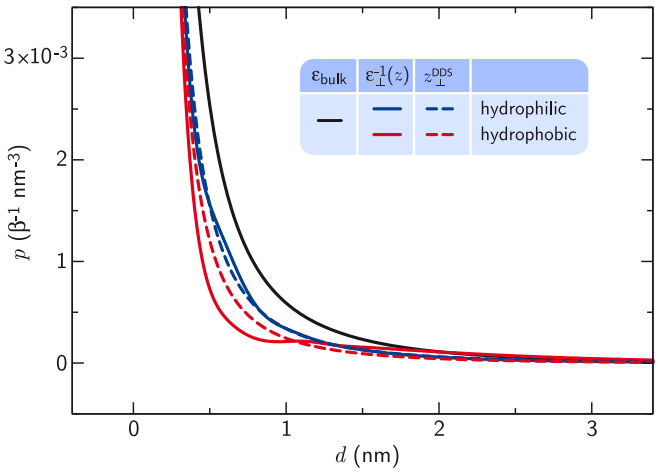

Figure 14: Pressure between two like-charged hydrophilic and hydrophobic plates as a function of the distance d between the plates, calculated from Eqs. 55 and 56 using different models for the dielectric profiles $\varepsilon_\perp^{-1}(z)$. The surface charge density is $\sigma_0 = -0.006\ e\ {\rm nm}^{-2}$.

of charged surfaces, the hydration repulsion has been associated with dielectric effects [55]. This differs from our findings, according to which dielectric effects decrease the pressure between charged surfaces and therefore the hydration repulsion must come from solvation effects not directly connected to dielectric properties. Interestingly, the repulsion at short distances in Fig. 14 is found to be smaller between hydrophobic surfaces than between hydrophilic ones. It is important to note that the pressures derived from the modified Poisson-Boltzmann equation shown in Fig. 14 do not include hydration or solvophobic effects and consequently vanish for zero surface charge density; so the message is that the dielectric profile cannot explain the hydration repulsion (which acts also between neutral surfaces) but nevertheless influences the electrostatic part of the double-layer pressure, and in fact makes the pressure between similarly charged surfaces less repulsive.

► **Ion-surface interactions.** Correlated electrostatic effects such as the image charge repulsion at a dielectric boundary cannot be treated on the mean-field level. However, for a single, finite-sized ion crossing a dielectric boundary, the image charge repulsion has been calculated in Refs. [56, 57], involving the effective dielectric radius of the ion. Tentatively, free energies calculated this way may be included as a correction to the mean-field potential similar to the heuristic potential $\mu_\pm(z)$. The image charge repulsion depends on the ionic radius, but ionic radii inferred from crystal structures are too small and consistently overestimate hydration free energies. To reproduce the Born solvation free energy, the distance between the ion and the first water dipole has to be added to the crystal radius as explained in Refs. [58, 59] and references therein. Motivated by our results for the planar interface, which show that density

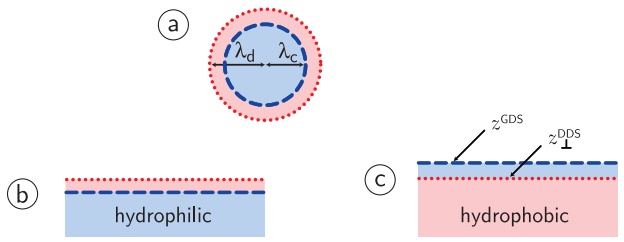

Figure 15: (a) Sketch of an ion with cavity radius λ_c (blue dashed line) and dielectric radius λ_d (red dotted line). Also shown are sketches of (b) a hydrophilic and (c) a hydrophobic surface with their respective Gibbs (blue dashed lines) and dielectric dividing surfaces (red dotted lines).

and dielectric properties give rise to two distinct and largely independent length scales, we propose a model for the ionic interaction with surfaces that distinguishes between dielectric and nonelectrostatic solvation-induced ion-surface interactions. Similar to the Gibbs and dielectric dividing surfaces at planar interfaces, we introduce the ionic cavity radius λ_c and the dielectric radius λ_d, see Fig. 15. The expression for the image potential is taken directly from Ref. [57]. We define the distance to the dielectric dividing surface position $z_\perp^{DDS}$ as $z' = z - z_\perp^{DDS}$. For $z' > \lambda_d$, the image potential of a monovalent ion is given by

$$U_i(z') = \frac{\beta e^2}{32\pi\,\lambda_d\,\varepsilon_0\varepsilon_1}\left[4 + \frac{(\varepsilon_1-\varepsilon_2)}{(\varepsilon_1+\varepsilon_2)}\frac{2\lambda_d}{z'} + \frac{(\varepsilon_1-\varepsilon_2)^2}{(\varepsilon_1+\varepsilon_2)^2}\left(\frac{2\lambda_d^2}{\lambda_d^2-(2z')^2} + \frac{\lambda_d}{2z'}\ln\frac{2z'+\lambda_d}{2z'-\lambda_d}\right)\right], \tag{57}$$

and for $0 < z' < \lambda_d$ by

$$U_i(z') = \frac{\beta e^2}{32\pi\,\lambda_d\,\varepsilon_0\varepsilon_1}\left[2 + \frac{2z'}{\lambda_d} + \frac{\varepsilon_1-\varepsilon_2}{\varepsilon_1+\varepsilon_2}\left(4 - \frac{2z'}{\lambda_d}\right) + \frac{(\varepsilon_1-\varepsilon_2)^2}{(\varepsilon_1+\varepsilon_2)^2}\left[\frac{(\lambda_d+z')(\lambda_d-2z')}{\lambda_d^2+2z'\lambda_d} + \frac{\lambda_d}{2z'}\ln\frac{2z'+\lambda_d}{\lambda_d}\right]\right] + \frac{\beta e^2}{16\pi\,\lambda_d\,\varepsilon_0\varepsilon_2}\left(\frac{2\varepsilon_2}{\varepsilon_1+\varepsilon_2}\right)^2\left(1 - \frac{z'}{\lambda_d}\right). \tag{58}$$

The permittivities are $\varepsilon_1 = \varepsilon_{bulk}$ and $\varepsilon_2 = 1$ for $z' > 0$. For $z' < 0$, the same expressions can be used with $\varepsilon_1 = 1$ and $\varepsilon_2 = \varepsilon_{bulk}$. Because we calculate the energy with respect to a position in the bulk water, we subtract the Born energy $U_b = e^2/8\pi\lambda_d\varepsilon_0\varepsilon_{bulk}$ from U_i. In addition to the image potential, the ions are subject to a hydration potential, scaling with the hydrated volume of the ion [60, 61, 62, 63]. To calculate the ionic volume, we use the cavity radius λ_c. Whereas the image potential acts with respect to the dielectric dividing surface, the hydration potential acts with respect to the Gibbs dividing surface. These surface positions appear in different order at hydrophilic and hydrophobic surfaces. The hydration energy is calculated from

$$U_h(z'') = \begin{cases} -\frac{4\pi}{3}\lambda_c^3\beta C & \text{if } z'' < -\lambda_c \\ 0 & \text{if } z'' > \lambda_c \\ -\frac{\pi}{3}(\lambda_c - z'')^2(z''+2\lambda_c)\,\beta C & \text{otherwise,} \end{cases} \tag{59}$$

with $z'' = z - z^{GDS}$ and $C = 2.8\times10^{-19}$ J/nm^3 [60]. We calculate the interaction potential of a single ion next to a dielectric boundary as the sum of the hydration energy and the image potential, $U(z) = U_h(z) + U_i(z) - U_b$.

In Fig. 16 we plot the calculated energy as a function of z for (a) a hydrophilic surface and (b) a hydrophobic surface, for a small and a big ion. For the small ion, the cavity radius $\lambda_c = 0.15$ nm and the dielectric radius $\lambda_d = 0.25$ nm, and for the big ion $\lambda_c = 0.2$ nm and $\lambda_d = 0.3$ nm. We choose the dielectric radii larger than the cavity radii, reflecting the fact that radii inferred from the solvation free energy via the Born energy U_b are larger than cavity radii measured with diffraction methods [59]. It also conforms to our result that the dielectric dividing surface is displaced towards the water phase compared to the Gibbs dividing surface at hydrophilic surfaces. The curves clearly reflect the well-known positive correlation between ion size and adsorption onto the surface, meaning that larger ions show a larger surface propensity compared to small ions. Interestingly, this simple model already shows a striking difference between hydrophilic and hydrophobic surfaces, which has recently been found in simulations as well [64]. Because $z^{GDS} > z_\perp^{DDS}$ at the hydrophobic surface, the influence of the attractive hydration potential is much more pronounced than at the hydrophilic surface. For ions of $\lambda_c = 0.2$ nm, the hydration potential at the hydrophobic surface even dominates the interaction for $0.09 < z < 0.26$ nm, which means that big ions adsorb onto hydrophobic surfaces, but not onto hydrophilic surfaces. For distances of ~ 0.3 nm from the interface, all potentials resemble the exponential function used previously for $\mu_\pm(z)$.

5 Conclusion

We have established the theoretical framework to calculate the dielectric response tensor at an interface from molecular fluctuations and from an applied external field. Whereas the parallel response can be calculated from the dipole moment only and roughly follows the density profile, the perpendicular response exhibits several singularities that can only be captured properly when higher-order multipole moments are taken into account. For the perpendicular dielectric response, the linear response regime extends to an external field strength of at least $D_\perp/\varepsilon_0 =\sim 2$ V/nm, after which the response at the hydrophobic interface becomes nonlinear. Because

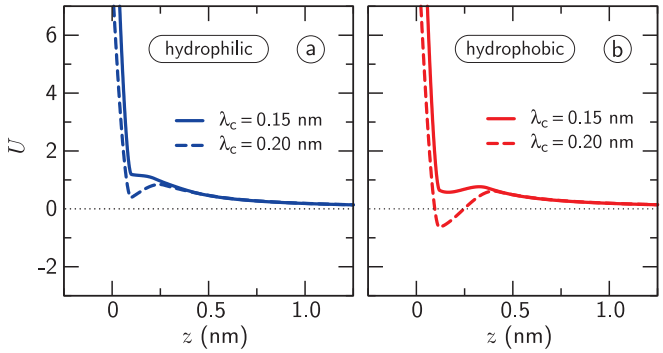

Figure 16: Ionic free energy $U(z) = U_h(z) + U_i(z) - U_b$ at (a) a hydrophilic surface and (b) a hydrophobic surface, calculated from Eqs. 57-59. At the hydrophilic surface $z_\perp^{\mathrm{DDS}} = 0.10$ nm and $z^{\mathrm{GDS}} = 0.07$ nm, at the hydrophobic surface $z_\perp^{\mathrm{DDS}} = 0.12$ nm and $z^{\mathrm{GDS}} = 0.22$ nm. The ions have a cavity radius of $\lambda_c = 0.15$ nm and $\lambda_c = 0.2$ nm and the dielectric radii λ_d are 0.1 nm larger.

at timescales larger than ~ 10 ns, dielectric breakdown in real water occurs at field strengths one order of magnitude lower, the nonlinear response of the nonpolarizable, nonionizable water model that we use in our simulations is not expected to play a role in the dielectric response of real water. Including the dielectric profile in a mean-field description of ion distributions at a charged interface, the experimental double-layer capacitance can be well reproduced. In particular, this shows that the Stern layer is predominantly caused by the dielectric interfacial features of water itself. Additionally accounting for the repulsive ion-substrate interaction, corresponding to steric exclusion of ions from the direct proximity of the wall, further improves the agreement with experimental data, but these direct ion-surface interactions are not decisive for the features seen in the experimental capacitance data. We quantify the difference between the dielectric response at hydrophilic and hydrophobic surfaces in terms of a single length scale that we call the dielectric dividing surface. Using this length scale, we find that the experimental similarity between the double-layer capacitance at both surface types can be rationalized very simply: although a pronounced depletion layer exists at the hydrophobic interface, and therefore less water is available than at the hydrophilic interface, the dielectric dividing surface position is very similar at both surface types, measured with respect to the top layer of heavy substrate atoms. In other words, water at the hydrophobic surface is a "better dielectric" than at the hydrophilic surface. From the same mean-field description, we find that the effect of the dielectric profile is to decrease the disjoining pressure between two charged plates. Dielectric interface effects therefore cannot explain the universally observed hydration repulsion between polar surfaces directly. Finally, a simple model for the adsorption of spherical ions at interfaces that distinguishes between dielectric and depletion effects, both at the planar interfaces and around the ions, reveals the characteristic difference between adsorption at hydrophilic and hydrophobic surfaces. In particular, it predicts the adsorption of large ions onto hydrophobic surfaces, but not onto hydrophilic surfaces. In future research, the effect of ions and finite surface separation on the dielectric profile and the consequences of the full dielectric profile on the ionic free energy need to be addressed in order to understand the interaction of charged and neutral surfaces in full detail.

Appendix

This Appendix contains an overview of published experimental values of the double-layer capacitance on various carbon-based surfaces in aqueous electrolytes. The capacitance of the electrical double layer is measured using cyclic voltametry or AC impedance spectroscopy. The accessible surface area is determined using N_2 adsorption.

In the tables below, we grouped the different measurements based on the contact angle in aqueous solution. When below 90°, the substrate is classified as hydrophilic (listed in Tab. A1), otherwise as hydrophobic (listed in Tab. A2). Materials of which the contact angle is unknown or unclear are displayed in Tab. A3. All data are plotted as a function of electrolyte concentration in Fig. A1. The scattering in the data between substrates and electrolytes is larger than the structural difference between hydrophilic and hydrophobic substrates. Nevertheless, when a specific substrate is modified to become more hydrophilic, for example using functional groups or doping, the double-layer capacitance increases [50, 65]. In addition, we show the limiting "bulk" value of the differential double-layer capacitance $C = \mathrm{d}\sigma_0/\mathrm{d}\psi_0$, calculated from the Debye-Hückel equation (Eq. 53, using the bulk dielectric constant $\varepsilon_\perp^{-1}(z) = \varepsilon_{\mathrm{bulk}}^{-1}$ with $\varepsilon_{\mathrm{bulk}} = 71$ for the entire fluid and $\mu(z) = 0$). For all substrates, the capacitance is much lower than the bulk value.

Many of the materials used for double-layer capacitors belong to the class of so-called activated carbons, which are treated with a gas plasma or a strong acid or base solution to make the surface more porous. While increasing the total capacitance of the sample, activation of a carbon surface often decreases the capacitance per unit surface area dramatically [66, 67]. Although the mechanism leading to this decrease is unclear, we can safely assume that a part of the additional surface area created by the activation process is inaccessible to the electrolyte, and therefore does not contribute to the double-layer capacitance. Because of these poorly defined surface characterisics, the experimental data on activated carbon substrates is discarded in our comparison, and Fig. 13 contains the data from Tabs. A2, A1 and A3 only.

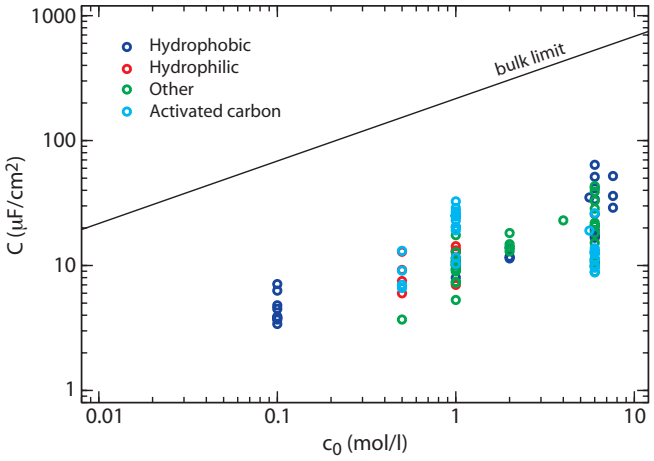

Figure A1: Double-layer capacitance as a function of bulk concentration, showing all data points from Tabs. A2, A1, A3 and A4, as well as the bulk value of the capacitance, calculated using $\varepsilon_{\text{bulk}} = 71$ and $\mu(z) = 0$.

Table A1: Double-layer capacitance of hydrophilic carbon-based materials.

Surface material	Contact angle (°)	Electrolyte	Concentration (M)	Capacitance (μF/cm^2)	Ref.
Carbon fibers	24 - 37 [68]	H_2SO_4	0.5	6.0 7.5 9.2 12.9	[69][a]
Carbon-coated Al_2O_3	57	H_2SO_4	1	7.0	[65]
Nitrogen-doped	41			11.4	
Boron-doped	60			12.9	
Oxidated polyvinylpyridine	45 - 67	H_2SO_4	1	13.2	[70]
Blend with coal tar pitch	[71, 72]			14.3	

[a]Different values correspond to different commercial samples (untreated).

Table A2: Double-layer capacitance of hydrophobic carbon-based materials.

Surface material	Contact angle (°)	Electrolyte	Concentration (M)	Capacitance (μF/cm^2)	Ref.
Boron-doped diamond	> 90 [73]	H_2SO_4	0.1	3.7	[74][a]
				7.1	
		KCl	0.1	3.4	
				4.5	
		$NaNO_3$	0.1	3.8	
				6.3	
		NaOH	0.1	3.9	
				4.8	
Carbide-derived carbon	> 90 [75]	H_2SO_4	2	11.4	[76]
TiC, TiC & SiC/TiC				13.8	
				11.8	
Graphite	98 [77]	KOH	6	17.5	[78][b]
				16.7	
				19.2	
				25.9	
				33.9	
				41.6	
				51.4	
				64.0	
Graphene nanosheets	127 [77]	KOH	7.6	29	[79]
				26	
				52	
Carbon black		H_2SO_4	1	8	[80]
Graphite powder		NaCl	5.6	35	

[a] The different values correspond to AC impedance and cyclic voltametry measurements, respectively.
[b] The surface area of natural graphite was increased using ball-milling; different values correspond to different milling times.

Table A3: Double-layer capacitance of materials with unknown contact angle.

Surface material	Electrolyte	Concentration (M)	Capacitance (μF/cm^2)	Ref.
Porous carbon	H_2SO_4	1	5.3	[81]
Porous carbon with polyaniline			9.0	
Silica-templated mesoporous carbon	H_2SO_4	1	12.8	[70]
			10.1	
			7.4	
			9.3	
			11.4	
			9.4	
Silica-templated mesoporous carbon	H_2SO_4	1	7.3	[82]
		2	14	[83]
		2	13	[84]
Silica-templated mesoporous carbon	H_2SO_4	1	10.2	[85]
			10.6	
			10.7	
			10.9	
	KOH	6	9.8	
			10.9	
			8.9	
			10.6	
Mesoporous carbon with NiO	KOH	2	18.2	[86]
Carbon aerogel	KOH	4	23	[80]
	KOH	6	28.5	[87]
Porous carbon	KOH	6	33	[67]
Self-ordered mesoporous carbon	$LiPF_6$	1	10	[88]
Nitrogen-containing mesoporous carbon	KOH	6	39.2	[66]
Ordered mesoporous carbon			10.0	
Porous carbon from cabonization	KOH	6	20.8	[89]
of poly(vinylidene chloride)			22.0	
			20.8	
			18.2	
			15.2	
			12.9	
Diamond film	NaCl	0.5	3.7	[90][a]
Polyacrylonitrile	H_2SO_4	1	24.9	[70]
Blend with coal tar pitch			20.3	
			17.5	
TiC/TiO_2	H_2SO_4	2	14.8	[76]
Carbon composite from waste paper	KOH	6	43.2	[87]

[a] After equilibration in electrolyte, assuming complete wetting at the maximum of the capacitance.

Table A4: Double-layer capacitance of different kinds of activated carbons.

Surface material	Electrolyte	Concentration (M)	Capacitance (μF/cm^2)	Ref.
CO_2 activated porous carbon	KOH	6	13	[67]
			9.6	
KOH activated porous carbon			10	
			8.8	
Nitrogen-containing mesoporous	KOH	6	26.2	[66]
carbon, activated with KOH			13.7	
			11.3	
Ordered mesoporous carbon,	KOH	6	11.2	[66]
activated with KOH			12.7	
			12.4	
KOH-activated carbon	H_2SO_4	1	20.4	[91]
			25.1	
			26.9	
NaOH-activated carbon			24.7	
			25.0	
			28.9	
Wood origin HNO_3-activated carbon	H_2SO_4	1	11.6	[92]
			10.3	
			19.1	
			25.5	
			23.0	
			32.6	
Activated carbon	NaCl	5.6	19	[80]
O_2-activated carbon fibers			6.6	[69]
			7.0	
			9.1	
			13.2	

References

[1] Israelachvili, J. & Wennerström, H. Role of hydration and water structure in biological and colloidal interactions. *Nature* **379**, 219 (1996).

[2] Benjamin, I. Chemical reactions and solvation at liquid interfaces: A microscopic perspective. *Chem. Rev.* **96**, 1449 (1996).

[3] Marčelja, S. & Radić, N. Repulsion of interfaces due to boundary water. *Chem. Phys. Lett.* **42**, 129 (1976).

[4] Marčelja, S. *et al.* Role of solvent structure in solution theory. *J. Chem. Soc. Faraday Trans. II* **73**, 630 (1977).

[5] Ball, P. Chemical physics: How to keep dry in water. *Nature* **423**, 25 (2003).

[6] Chandler, D. Interfaces and the driving force of hydrophobic assembly. *Nature* **437**, 640 (2005).

[7] Kornyshev, A. A., Schmickler, W. & Vorotyntsev, M. A. Nonlocal electrostatic approach to the problem of a double layer at a metal-electrolyte interface. *Phys. Rev. B* **25**, 5244 (1982).

[8] Kornyshev, A. A. & Vorotyntsev, M. A. Nonlocal dielectric response of the electrode-solvent interface in the double-layer problem. *Can. J. Chem.* **59**, 2031 (1981).

[9] Kornyshev, A. A., Spohr, E. & Vorotyntsev, M. A. *Electrochemical Interfaces: At the Border Line*, chap. 2.1, 33 (Wiley, New York, 2002).

[10] Bopp, P. A., Kornyshev, A. A. & Sutmann, G. Frequency and wave-vector dependent dielectric function of water: Collective modes and relaxation spectra. *J. Chem. Phys.* **109**, 1939 (1998).

[11] Lyklema, J. *Fundamentals of Interface and Colloid Science*, vol. II (Academic Press, London, 1995).

[12] Hunter, R. J. *Foundations of Colloid Science* (Oxford University Press, Oxford, 2001), second edn.

[13] Stern, O. Zur Theorie der elektrolytischen Doppelschicht. *Z. Elektrochem.* **30**, 508 (1924).

[14] Bonthuis, D. J., Gekle, S. & Netz, R. R. Dielectric profile of interfacial water and its effect on double-layer capacitance. *Phys. Rev. Lett.* **107**, 166102 (2011).

[15] Hasted, J. B., Ritson, D. M. & Collie, C. H. Dielectric properties of aqueous ionic solutions. *J. Chem. Phys.* **16**, 1 (1948).

[16] Grahame, D. C. Effects of dielectric saturation upon the diffuse double layer and the free energy of hydration of ions. *J. Chem. Phys.* **18**, 903 (1950).

[17] Heugen, U. *et al.* Solute-induced retardation of water dynamics probed directly by terahertz spectroscopy. *Proc. Nat. Acad. Sci. USA* **103**, 12301 (2006).

[18] Tielrooij, K. J. *et al.* Dielectric relaxation dynamics of water in model membranes probed by terahertz spectroscopy. *Biophysical J.* **97**, 2484 (2009).

[19] Blum, L. & Henderson, D. Mixtures of hard ions and dipoles against a charged wall - the Ornstein-Zernike equation, some exact results, and the mean spherical approximation. *J. Chem. Phys.* **74**, 1902 (1981).

[20] Abrashkin, A., Andelman, D. & Orland, H. Dipolar Poisson-Boltzmann equation: Ions and dipoles close to charge interfaces. *Phys. Rev. Lett.* **99**, 077801 (2007).

[21] Paillusson, F. & Blossey, R. Slits, plates, and Poisson-Boltzmann theory in a local formulation of nonlocal electrostatics. *Phys. Rev. E* **82**, 052501 (2010).

[22] Frenkel, J. *Kinetic Theory of Liquids* (Dover Publications, New York, 1955).

[23] Stillinger, F. H. & Ben-Naim, A. Liquid-vapor interface potential for water. *J. Chem. Phys.* **47**, 4431 (1967).

[24] Shen, Y. R. & Ostroverkhof, V. Sum-frequency vibrational spectroscopy on water interfaces: Polar orientation of water molecules at interfaces. *Chem. Rev.* **106**, 1140 (2006).

[25] Ballenegger, V. & Hansen, J. Local dielectric permittivity near an interface. *Europhys. Lett.* **63**, 381 (2003).

[26] Kharkats, Y. I., Kornyshev, A. A. & Vorotyntsev, M. A. Electrostatic models in theory of solutions. *J. Chem. Soc. Faraday Trans. II* **72**, 361 (1976).

[27] Noyes, R. M. Thermodynamics of ion hydration as a measure of effective dielectric properties of water. *J. Am. Chem. Soc.* **84**, 513 (1962).

[28] Fedorov, M. V. & Kornyshev, A. A. Unravelling the solvent response to neutral and charged solutes. *Mol. Phys.* **105**, 1 (2007).

[29] Levin, Y. Polarizable ions at interfaces. *Phys. Rev. Lett.* **102**, 147803 (2009).

[30] Leikin, S., Parsegian, V. A., Rau, D. C. & Rand, R. P. Hydration forces. *Annu. Rev. Phys. Chem.* **44**, 369 (1993).

[31] Jackson, J. D. *Classical Electrodynamics* (John Wiley & Sons, USA, 1998), third edn.

[32] Russakoff, G. Derivation of macroscopic Maxwell equations. *Am. J. Physics* **38**, 1188 (1970).

[33] Kirkwood, J. G. The dielectric polarization of polar liquids. *J. Chem. Phys.* **7**, 911 (1939).

[34] Fröhlich, H. *Theory of Dielectrics* (Clarendon Press, Oxford, 1949).

[35] Ballenegger, V. & Hansen, J. Dielectric permittivity profiles of confined polar fluids. *J. Chem. Phys.* **122**, 114711 (2005).

[36] Lindahl, E., Hess, B. & Van der Spoel, D. GROMACS 3.0: a package for molecular simulation and trajectory analysis. *J. Mol. Mod.* **7**, 306 (2001).

[37] Sendner, C., Horinek, D., Bocquet, L. & Netz, R. R. Interfacial water at hydrophobic and hydrophilic surfaces: Slip, viscosity, and diffusion. *Langmuir* **25**, 10768 (2009).

[38] Abascal, J. L. F. & Vega, C. A general purpose model for the condensed phases of water: TIP4P/2005. *J. Chem. Phys.* **123**, 234505 (2005).

[39] Sedlmeier, F., Horinek, D. & Netz, R. R. Spatial correlations of density and structural fluctuations in liquid water: A comparative simulation study. *J. Am. Chem. Soc.* **133**, 1391 (2011).

[40] Reddy, M. R. & Berkowitz, M. The dielectric constant of SPC/E water. *Chem. Phys. Lett.* **155**, 173 (1989).

[41] Fedorov, M. V. & Kornyshev, A. A. Towards understanding the structure and capacitance of electrical double layer in ionic liquids. *Electrochim. Acta.* **53**, 6835 (2008).

[42] Bazant, M. Z., Storey, B. D. & Kornyshev, A. A. Double layer in ionic liquids: Overscreening versus crowding. *Phys. Rev. Lett.* **106**, 046102 (2011).

[43] Kolb, J. F., Joshi, R. P., Xiao, S. & Schoenbach, K. H. Streamers in water and other dielectric liquids. *J. Phys. D: Appl. Phys.* **41**, 234007 (2008).

[44] Paluch, M. Electrical properties of free surface of water and aqueous solutions. *Adv. Colloid Interface Sci.* **84**, 27 (2000).

[45] Du, Q., Superfine, R., Freysz, E. & Shen, Y. R. Vibrational spectroscopy of water at the vapor water interface. *Phys. Rev. Lett.* **70**, 2313 (1993).

[46] Du, Q., Freysz, E. & Shen, Y. R. Vibrational spectra of water molecules at quartz/water interfaces. *Phys. Rev. Lett.* **72**, 238 (1994).

[47] Du, Q., Freysz, E. & Shen, Y. R. Surface vibrational spectroscopic studies of hydrogen bonding and hydrophobicity. *Science* **264**, 826 (1994).

[48] Wilson, M. A., Pohorille, A. & Pratt, L. R. Study on the liquid vapor interface of water. 1: Simulation results of thermodynamic properties and orientational structure. *J. Chem. Phys.* **90**, 5211 (1989).

[49] Sokhan, V. P. & Tildesley, D. J. The free surface of water: molecular orientation, surface potential and nonlinear susceptibility. *Mol. Phys.* **92**, 625 (1997).

[50] Kim, Y.-T. *et al.* Drastic change of electric double layer capacitance by surface functionalization of carbon nanotubes. *Applied Phys. Lett.* **87**, 234106 (2005).

[51] Lyklema, J. *Fundamentals of Interface and Colloid Science*, vol. I (Academic Press, London, 1991).

[52] Andelman, D. *Introduction to Electrostatics in Soft and Biological Matter*, chap. 6, 97 (Taylor & Francis, New York, 2006).

[53] Edwards, S. A. & Williams, D. R. M. Double layers and interparticle forces in colloid science and biology: Analytic results for the effect of ionic dispersion forces. *Phys. Rev. Lett.* **92**, 248303 (2004).

[54] Schneck, E. & Netz, R. R. From simple surface models to lipid membranes: Universal aspects of the hydration interaction from solvent-explicit simulations. *Curr. Opin. Colloid Interface Sci.* **16**, 607 (2011).

[55] Faraudo, J. & Bresme, F. Origin of the short-range, strong repulsive force between ionic surfactant layers. *Phys. Rev. Lett.* **94**, 077802 (2005).

[56] Kharkats, Y. I. & Ulstrup, J. The electrostatic Gibbs energy of finite-size ions near a planar boundary between 2 dielectric media. *J. Electroanal. Chem.* **308**, 17 (1991).

[57] Markin, V. S. & Volkov, A. G. Quantitative theory of surface tension and surface potential of aqueous solutions of electrolytes. *J. Phys. Chem. B* **106**, 11810 (2002).

[58] Jayaram, B., Fine, R., Sharp, K. & Honig, B. Free-energy calculations of ion hydration - an analysis of the Born model in terms of microscopic simulations. *J. Phys. Chem.* **93**, 4320 (1989).

[59] Marcus, Y. Ionic radii in aqueous solutions. *Chem. Rev.* **88**, 1475 (1988).

[60] Huang, D. M., Cottin-Bizonne, C., Ybert, C. & Bocquet, L. Aqueous electrolytes near hydrophobic surfaces: Dynamic effects of ion specificity and hydrodynamic slip. *Langmuir* **24**, 1442 (2008).

[61] Horinek, D. *et al.* Specific ion adsorption at the air/water interface: The role of hydrophobic solvation. *Chem. Phys. Lett.* **479**, 173 (2009).

[62] Huang, D. M., Geissler, P. L. & Chandler, D. Scaling of hydrophobic solvation free energies. *J. Phys. Chem. B* **105**, 6704 (2001).

[63] Hummer, G., Garde, S., García, A. E., Paulaiti, M. E. & Pratt, L. R. Hydrophobic effects on a molecular scale. *J. Phys. Chem. B* **102**, 10469 (1998).

[64] Schwierz, N., Horinek, D. & Netz, R. R. Reversed anionic Hofmeister series: The interplay of surface charge and surface polarity. *Langmuir* **26**, 7370 (2010).

[65] Kwon, T. *et al.* Enhancement mechanism of electrochemical capacitance in nitrogen-/boron-doped carbons with uniform straight nanochannels. *Langmuir* **25**, 11961 (2009).

[66] Jiang, J. *et al.* Enhanced electrical capacitance of porous carbons by nitrogen enrichment and control of the pore structure. *Microporous Mesoporous Mater.* **118**, 28 (2009).

[67] Wang, H., Gao, Q. & Hu, J. Preparation of porous doped carbons and the high performance in electrochemical capacitors. *Microporous Mesoporous Mater.* **131**, 89 (2010).

[68] Artemenko, S. E., Glukhova, L. G. & Zagoruiko, N. I. Effect of oxidative treatment of carbon fibre on the properties of a carbon-fibre-filled plastic fabricated by polycondensation filling. *Fibre Chemistry* **33**, 502 (2001).

[69] Okajima, K., Ohta, K. & Sudoh, M. Capacitance behavior of activated carbon fibers with oxygen-plasma treatment. *Electrochim. Acta* **50**, 2227 (2005).

[70] Frackowiak, E. *et al.* Optimisation of supercapacitors using carbons with controlled nanotexture and nitrogen content. *Electrochim. Acta* **51**, 2209 (2006).

[71] Sidorenko, A. *et al.* Switching of polymer brushes. *Langmuir* **15**, 8349 (1999).

[72] Harnish, B. *et al.* UV-cross-linked poly(vinylpyridine) thin films as reversibly responsive surfaces. *Chem. Mater.* **17**, 4092 (2005).

[73] Goeting, C. H. *et al.* Sonoelectrochemistry at tungsten-supported boron-doped CVD diamond electrodes. *Diamond Relat. Mater.* **8**, 824 (1999).

[74] Swain, G. M. & Ramesham, R. The electrochemical activity of boron-doped polycrystalline diamond thin-film electrodes. *Anal. Chem.* **65**, 345 (1993).

[75] Kocrick, E. *et al.* Ordered mesoporous carbide derived carbons for high pressure gas storage. *Carbon* **48**, 1707 (2010).

[76] Fernández, J. A. *et al.* EDLC performance of carbide-derived carbons in aprotic and acidic electrolytes. *Electrochim. Acta* **53**, 7111 (2008).

[77] Wang, S. *et al.* Wettability and surface free energy of graphene films. *Langmuir* **25**, 11078 (2009).

[78] Li, H.-Q. *et al.* A competitive candidate material for aqueous supercapacitors: High surface-area graphite. *J. Power Sources* **185**, 1557 (2008).

[79] Du, X. *et al.* Graphene nanosheets as electrode material for electric double-layer capacitors. *Electrochim. Acta* **55**, 4812 (2010).

[80] Pandolfo, A. G. & Hollenkamp, A. F. Carbon properties and their role in supercapacitors. *J. Power Sources* **157**, 11 (2006).

[81] Chen, W.-C. & Wen, T.-C. Electrochemical and capacitive properties of polyaniline-implanted porous carbon electrode for supercapacitors. *J. Power Sources* **117**, 273 (2003).

[82] Karandikar, P. *et al.* Synthesis and characterization of mesoporous carbon through inexpensive mesoporous silica as template. *Microporous Mesoporous Mater.* **98**, 189 (2007).

[83] Sevilla, M. *et al.* Performance of templated mesoporous carbons in supercapacitors. *Electrochim. Acta* **52**, 3207 (2007).

[84] Fuertes, A. B., Pica, F. & Rojo, J. M. Influence of pore structure on electric double-layer capacitance of template mesoporous carbons. *J. Power Sources* **133**, 329 (2004).

[85] Fuertes, A. B. *et al.* Templated mesoporous carbons for supercapacitor application. *Electrochim. Acta* **50**, 2799 (2005).

[86] Cao, Y. *et al.* Synthesis, characterization, and electrochemical properties of ordered mesoporous carbons containing nickel oxide nanoparticles using sucrose and nickel acetate in a silica template. *J. Solid State Chem.* **180**, 792 (2007).

[87] Kalpana, D. *et al.* Recycled waste paper - a new source of raw material for electric double-layer capacitors. *J. Power Sources* **190**, 587 (2009).

[88] Zhou, H. *et al.* Electrochemical capacitance of self-ordered mesoporous carbon. *J. Power Sources* **122**, 219 (2003).

[89] Xu, B. *et al.* High-capacitance carbon electrode prepared by PVDC carbonization for aqueous EDLCs. *Electrochim. Acta* **54**, 2185 (2009).

[90] Ramesham, R. & Rose, M. F. Electrochemical characterization of doped and undoped CVD diamond deposited by microwave plasma. *Diamond Relat. Mater.* **6**, 17 (1997).

[91] Roldán, S. *et al.* Comparison between electrochemical capacitors based on NaOH- and KOH-activated carbons. *Energy Fuels* **24**, 3422 (2010).

[92] Seredych, M. *et al.* Surface functional groups of carbons and the effects of their chemical character, density and accessibility to ions on electrochemical performance. *Carbon* **46**, 1475 (2008).